Dear Ms. Werban,

thank you for giving us the opportunity to revise our manuscript. We thank the reviewers for their comments and constructive suggestions, which we considered in detail to improve the presentation of our study. Please find below our point-by-point response to the *original comments*:

1 Reviewer 1 (Hendy Setiawan)

1. *page 8, line 29: The safety factor of $F_S < 1.5$ for unstable hillslopes, is this statement applied for seismic induced, or rainfall-induced or both in general?*

   In this particular case we refer to the work by Chen et al. [2017]. They mentioned both rainfall and earthquakes for their safety factor definition.

   Changes in text (p. 9, l. 3):

   Chen et al. [2017] characterized unstable hillslopes, related to both rainfall and earthquakes, by a safety factor of $FS < 1.5$. Rarely is the limit equilibrium at $FS = 1$ considered as a reliable metric in engineering geology.

2. *page 9 line 7–8: please check the equation of Arias intensity, is it $\frac{\pi}{2g}$ or $\frac{2}{\pi g}$, see reference i.e Jibson (2007), USGS (1993) or Stafford et al (2009).*

   This was a typo in the fraction indeed.

   Now changed in text (p. 9, l. 14):

   $\frac{\pi}{2g}$

3. *Page 10 line 6: please add remark M_0 for the seismic moment directly. Some equations remarks also should be checked and added (if not yet mentioned).*

   Done and changed in text (p. 10, l. 11):

   where $\Delta\sigma$ is the stress drop, μ the shear modulus, and M_0 the seismic moment.

4. *page 13, line 1: "...since energy is proportional to the seismic moment M_0 (Eq.9)..." this should be (Eq.10)?? (Hanks and Kanamori, 1979).*

   Yes, changed to Eq. 10. on p. 10, l. 10

5. *Page 13 line 12: "... and θ_E and θ_E are the azimuths of the maximum." This should be θ_E and θ_I*

   Yes, changed to θ_I on p. 13, l. 29

6. *Figure 14 indicates that mostly landslides concentrated in the aspect of about 120 degrees, south-east, with distance for the rupture approximately within 1–2 km, which from location densely surrounding Aso caldera. Besides rupture effects, does distinctive lithology condition in Aso caldera itself also contribute to this finding?*

The lithology (or at least the nominal descriptions of dominant rock types) does not show any distinctive directional properties. While it is reasonable to assume that landslides occurred along the weak zones (such as the Halloysite layers we refer to), no preferred orientation has been reported for these shallow layers. [Paudel et al., 2007, 2008, Sato et al., 2017].

7. *Does the rupture propagation energy also (at the end) include the compressional waves (page 9 line 24) in the Aso caldera, south-east side, where the landslides densely concentrated as described in your finding? What is your opinion as an additional explanation in the Discussion? Since your manuscript only applies the shear waves only for estimating the energy in the model.*

   The exact calculation of radiated seismic energy is quite complex, which is the main reason why we only consider the shear wave velocity at a site. Our assumption is that we treat the entire waveform as if it arrived at a constant velocity at a site when estimating the radiated seismic energy. This assumption results in an underestimation of the energy of 2.6% at longer distances and 7% at the fault. Compared to other components of the energy estimation procedure, e.g. the assumptions for the geometrical spreading, the usage of the shear wave velocity only introduces a minor error at most sites.

   Changed in text (p. 10, l. 11-16):

   Since most seismic energy is released as shear waves, we apply the shear wave velocity at the recording site (v_S) to the entire waveform, i.e. we assume that all waves arrive with velocity v_S at a site. This assumption has the advantage that it does not require a separation of the record into P- and S-waveforms, simplifying the computation. In the Appendix we show from a theoretical perspective that using a uniform v_S has only a small impact on the overall energy estimate.

   We added the detailed description of the appendix.

8. *Related to questions 6 and 7, after your findings, do the normal faulting component should be accounted into your model? For example, if we look both at strike-slip and normal components. Does it significantly affect the spatial pattern, asymmetrical distribution or landslides depth?*

   We showed that the fault-normal/fault-parallel ratios are consistent with Somerville et al. [1997], who also formulated their fault-normal/fault-parallel ratio as a term that can be easily plugged into a GMPE. Somerville et al. [1997] also provide model coefficients for fault-normal/fault-parallel ratios for dip-slip events. They observed a similar behaviour for strike-slip and dip-slip events with the dip-slip events exhibiting lesser amplitude variations of fault-normal/fault-parallel ratios and directivity. The formulation of the FN/FP term as an additional (optional) term for GMPEs is common practice [Somerville et al., 1997, Spudich et al., 2004, 2013]. Any impact of single components from strike-slip and normal faulting cannot be quantified here as we investigated only a single earthquake. Concerning the landslide depths, please see the next comment.

9. *Landslides aspects and asymmetric spatial distribution are well described in your manuscript. Do the depth variability of those recorded co-seismic landslides also can be related with the rupture propagation processes and can be explained through your physical-based ground motion model?*

   Unfortunately, we do not have depth measurements of the landslides. We only know that the coseismic landslides were shallow [Song et al., 2017, Sato et al., 2017, Hung et al., 2017], thus we cannot make a detailed statement about the relation between landslide depth and rupture processes. We could use an empirical scaling between landslide volume and area, but that would introduce additional (and unnecessary) scatter to our model.

2 Reviewer 2 (Qiang Xu)

1. *The unspecified landslide date are from NIED. Please discuss the possible uncertainties may cause by these data. In addition, how accuracy the coseismic inventory is, please also explain the possible mapping errors, and discuss how they will affect the results.*

   The landslides were mapped from aerial imagery at much higher resolution (sub-meter resolution) than the 30-m DEM that we used to compute local hillslope aspect and slope. Even a large systematic bias (up to several meters) in the landslide mapping would be small compared to the DEM resolution. We appreciate the reviewer's comment in this regard, but feel that a detailed uncertainty analysis of the landslide inventories is beyond the scope of this study.

2. *Figure 4: lines are not so visible. Fig.4 b and d are not well explained. Please use a better presentation of the data in this figure.*

   The figure has been modified to offer more detailed description and an explanatory figure.

3. *Figure 7: The explanation of this figure in the texts is not enough. Is this point density map? Do you consider the size of the landslides here?*

   Yes, these are kernel density maps of the landslides. The landslide area is taken into account in these figures as highlighted by the colorbar annotation. We added some more detail to the description of Fig. 7.

4. *Please explain the correlation between the unspecified landslides and the coseismic landslides? Are there any reactivations?*

   We discuss the relation between both landslide data sets at the end of the section "Topographic analysis". A detailed study of the unspecified and coseismic landslides is that by Chen et al. [2017], who reported 29 reactivated landslides in the area affected by slope failures. We refer to their work in the text.

Changed in text (p. 18, l.3):

Chen et al. [2017] identified only 29 landslide recactivations during the Kumamoto earthquake.

5. *Some relevant and important references are missing: Fan X et al (2018), published on Landslides journal: Coseismic landslides triggered by the 8th August 2017 Ms 7.0 Jiuzhaigou earthquake (Sichuan, China): factors controlling their spatial distribution and implications for the seismogenic blind fault identification.*

   We added the suggested reference to the introduction, page 1 line 23 and page 3 line 10.

6. *On Page 3, line 8-9: Wenchuan earthquake has been well studied by many others, please also refer to: Huang and Fan (2013). The landslide story on Nature Geoscience.*

   We agree with the reviewer: literally hundreds of papers on the Wenchuan earthquake have become available by now. Yet the suggested reference cites papers that we already cite concerning the earthquake related landslides of Wenchuan, i.e. Gorum et al. [2011].

3 Reviewer 3 (Tao Wang)

1. *In Figure 1 and 5, it is not obvious that Mt. Aso, its caldera, Mt. Shutendoji, Mt. Kinpo and Mt. Otake are near-identical conditions, particularly, the lithology, and topographic characteristics.*

   We used the term "near-identical condition" to outline that the four mountains have all geological young volcanic rocks of similar composition, and that hillslope inclination and MAF are elevated.

2. *In Figure 1, its true that the landslides triggered by this earthquake are concentrated mainly inside the caldera and the flanks of Mt. Aso. But this area is also nearer the fault rupture patch with highest slip than other three areas. This means more energy could be released from this place during the earthquake. So the difference between distance effect and directivity effect needs to be analyzed.*

   We agree on the statement that energy release is localized in the asperity. We address this by considering the asperity portion only and show the landslide distribution with asperity distance in a new figure (Fig. 5b) and landslide azimuth with respect to the asperity centroid (Fig 6b). Given the extent and steepness of the asperity patch, results change slighlty when compared to the results for the entire rupture plane.

3. *This directivity effect results in larger shaking amplitudes in the rupture propagation direction variations in wave amplitudes and energy related to the directivity effect occur at lower frequencies. The paper shows the total landslide affected area is within 22.9 km distance from the rupture plane. In this near fault area, the effect of high-frequency seismic ground motion on landslide should be more important than the low-frequency.*

   We partly agree on these statements, and see that some clarification is needed. We never stated that the lower-frequency contribution is more important; instead we say that it considerably contributes to the overall shaking and landslide triggering. The majority of landslides has aspects that cannot be explained solely by the lower-frequency ground motion and its associated directivity (Fig. 14). Because of these observations, we base our GMPE on Arias intensity. We also stated at the end of section 5.2 that the Arias intensity is more sensitive towards higher frequency contributions and that it explains most of the data, but not all of them. The ground motion contributions of the lower frequencies—related to energy—is lower than the ground motions at higher frequencies, as shown by our model. Adding an energy term helps to better explain ground motion, though it does by no means explain the entire ground motion. Considering the comments by the reviewer, we recognize that some of our statements are ambiguous. Hence, we made clearer statements in the conclusions.

   Changes in text (in page 27, lines 5-6, lines 13-15, lines 22-23.):

   We demonstrated that the pattern of coseismic landslides is not only consistent with ground motion at higher frequencies (e.g. distance dependence) but also contributions from lower frequencies are evident.

   We introduced a modified model for Arias intensity using site-dependent seismic energy estimates instead of the source-dependent seismic magnitude to better model low-frequency ground-motion in addition to the ground-motion at higher frequencies covered by the Arias intensity.

4. *The coseismic landslide is resulted in seismic load and slope geotechnical engineering conditions. This paper mainly makes an in-depth analysis from the engineering earthquake perspective, but the analysis of engineering geological factors is relatively rare. The conclusion is somehow different from some empirical knowledge. I suggest authors further analyze the influence of engineering geological factors. For example, authors can consider the physical and mechanical properties of rock-soil mass and DEM data with higher accuracy to analyze their correlation with landslide, and use quantitative indicators to describe the correlation. These may affect the results to some extent.*

   Our work focuses on the seismological part and less on the geological aspects, as these have been analyzed in detail by others for the Kumamoto region in context of the 2016 earthquake. Analysis of physical and mechanical properties of rock-soil mass has been conducted by several other authors [Dang et al., 2016, Song et al., 2017, Paudel et al., 2007, 2008, Sato et al., 2017] and we refer to those works accordingly. Including analyses concerning geotechnical factors at the same scale would expand the entire paper considerably, and is beyond the scope of a single publication and beyond our original objective. All metrics and methods are derived from accepted works in both geotechnical engineering and engineering seismology [e.g Harp and Wilson, 1995, Somerville et al., 1997]. One of our key results—the influence of rupture directivity on landslide patterns—has been speculated about in previous studies [e.g. Hovius and Meunier, 2012]. We also fail to see direct benefits of using a DEM of higher resolution and performing geotechnical analyses for the regional pattern of landsliding that we are interested in explaining. In any case, we use the DEM with highest resolution that is freely available for the region.

5. *Figure 1. Add a map scale and identify the epicenter of the Yufu event.*

   Like in the other maps, the map scale is now given in form of UTM coordinates and the event epicenter has been added.

6. *The location of mountain peaks should be shown in figure 2a. The details in the four areas listed in figure 5 should be evidenced by zooming in.*

   The mountain peaks haven been added to Fig. 2.

7. *Page 4. The map scale of the Seamless Digital Geological Map of Japan should be stated.*

   Yes, done.

   Changes in text (page 4, line 11-12):

   While data on major geological units are from the Seamless Digital Geological Map of Japan (scale 1:200,000) by the Geological Survey of Japan.

8. *Page 4. The computation process of fundamental frequency of hillslope section should be stated.*

   We do not compute the fundamental frequency; this is not necessary for the purpose of the computation of the median amplification factor (MAF). To avoid further confusion with the fundamental frequency of the hillslope, we deleted the following sentence: "The frequency f of the seismic wave is the fundamental frequency of the hillslope section on which landsliding occurred [Massa et al., 2014]." We see that this sentence might imply that MAF requires knowledge of the fundamental frequency of the hillslope. The frequency f as it used for the computation of MAF, is the frequency of the seismic wave.

9. *Page 8. Throughout the paper, no coseismic landslide displacement is calculated or used. I suggest delete this part.*

   We use the coseismic landslide displacement relation to show that it is related to acceleration and velocity, as our presented GMPE does. We clarified its purpose.

Changes in text (in page 9 lines 7-9):

Thus, the coseismic hillslope performance can be characterized by velocity and acceleration. In the following sections, we derive a ground-motion model based on the acceleration related Arias intensity and the velocity related radiated seismic energy.

10. *Page 11. Many empirical attenuation relationships for Arias intensity are developed recent years. Why use the Kramer (1996) model here?*

    As stated in the text, the functional form of Kramer [1996] is a template, and most ground motion prediction equations—including most recent ones—are related to it. We use the Kramer [1996] template function to highlight that our functional model does not differ from the bulk of other GMPEs. We clarified this and rewrote the first paragraph of the section related to the landslide related ground-motion models (page 13 lines 8-15).

4 Comments (Odin Marc)

1. *P8 L5-20 : In this paragraph I think you want to cite Marc et al 2016 (JGR about landslide total area and volume) and not Marc et al 2017 (about affected area).*

   Reference is corrected.

2. *P11 : L20 25 : the comparison of the 2 equations is a bit misleading because you add 2 terms (anelasic attenuation ,and Mw dependent geometric spreading c5), and shuffle the order : c3 becomes c4 in the second equation... Why not writing the second Eq : ln(I) = c1 + c2M + (c3+c4M)ln(r) + c6 r Also note that including anelastic attenuation has also been done in various studies (Meunier 2007, 2013, Yuan 2013) so it is not completely new. Nevertheless, I agree that it is often difficult to constrain the attenuation coefficient and thus, using geometric spreading only is often preferred.*

   The entire equation paragraph has been rephrased in more detail and the first equation uses now coefficients p_i that are compared and discussed with coefficients c_j of the second equation. The remarks on anelastic attenuation are now incorporated (page 13 lines 8-15). This refers also to the last comment.

3. *P14 L 11: indicating a landslide failure process starting from the crown and according to simulations by Dang et al. (2016). Sentence with a missing word ?*

   Indeed: indicating a landslide failure process starting from the crown and which is according to simulations by Dang et al. [2016].

4. *Fig 5 : Maybe indicate the Attenuation parameter obtained from the MLE exponetial fit ?*

   This comment is in connection to the comment for Fig. 9. The y-axis label reads now landslide concentration and is consistent now with Fig. 9, 12, 14, and 15. The figure has been reworked to account also for different distance metrics (rupture distance and asperity distance). The parameter estimates have been added to the figure.

5. *P15: L 1-9: Unclear what is the main message or aim of this paragraph. L1 Locations rather than localities ? L1 Propagated progressively : What do you mean? Are you talking about rupture propagation (as suggested by the following lines) or about run out (I.e landslide downslope, rapid, motion after failure). Because unless you specifically restrict analysis to scar areas the flatter areas are likely deposit areas, related to runout termination not rupture propagation.*

   This paragraph is specifically about the rupture process.

   The first sentence has been changed as follows in page 15 line 3:

   Most landslides originated at locations with amplified ground accelerations and steep hillslopes and propagated progressively to flatter areas with less amplified ground accelerations and deposited the material in areas of attenuated ground accelerations.

6. *L10 : Mt. Aso and its caldera and Mt. Shutendoji had a high density of landslides (Fig. 5), whereas Mt. Kinpo and Mt. Otake lack landslides, though these locations are closer to the epicenter and at comparable distances from the rupture (Fig. 5). Actually it is not so clear on Fig 5 (Aso is relatively low, similar to Otake). Referring to Fig 7 where the low spatial density is clearer (and adding Peak Names on this figure) may be better.*

   Another reviewer made similar remarks and the figures showing the peaks have been updated.

7. *Figure 4 : This is a nice ans standard figure. It may be worth to show the same figure done with the non EQ landslides ? That may be a simple to do supplementary figure that would show nicely if the trend in MAF is significant and due to the EQ (as there is no reason MAF should relate to rainfall induced landslides).*

   The NIED landslide inventory is unspecified with regard to the landslide trigger and we cannot extract the non-seismic landslides.

8. *Fig 6 very nice figure*

   Thanks!

9. *Fig 8: Density of landslide concentration is an awkward term. I guess it is the Kernel Density estimate of Landslide concentration (remind the unit of landslide concentration as in following figures)*

In Figure 9 (and Fig. 5 and 15 for that matter) the density is normalized to integrate to 1, while in figures 12 and 14 it scales to the landslide concentration, hence the different labels and units. Figure 5, 9 and 15 have been updated and the labeling and scaling is consistent with figures 12 and 14 with landslide concentration. This has implications on the parameters in Eq. 27 and 28 which have been accordingly updated.

10. *P20 L2 :depends on the ratio of rupture and shear wave velocity and the length of the rupture (Spudich and Chiou, 2008). Unless rediscussed later, it would be nice to know how: If fault length and rupture velocity indicates the ptotential importance of directivity for landslide pattern, it may be included in simple models.*

    The work of Spudich and Chiou [2008] explains in detail the procedure on how to use these parameters. Unfortunately, even their simplified model is relatively complex as it needs to account for the seismic radiation pattern. Describing it in more detail in this paper while not using the method would go too much off-topic and we have investigated one earthquake only here. Like the Somerville et al. [1997] model, it can be added as a term to existing GMPEs.

11. *Fig 11: On figure 11 I would have like to see the FN/FP in more details for the low frequency range. Indeed, how much of the variations in the 0.1-1Hz range remain in the 0.5-1Hz range ? Because we may expect the PGV/PGA at 0.1Hz too weak to cause landsliding, compare to the one between 0.5 and 1 Hz. If the authors can make it easily I would suggest they split the 0.1-1Hz range in 2 or 3 subplot, as it may yield useful insight for later studies on frequency effects on landslide triggering. Maybe as a supplementary figure, or as a few lines about the contribution of subranges of frequencies. This is somewhat shown in Fig 10 but as far as I understood Fig 10 is model and Fig 11 is data. The text is somewhat unclear about that and does not call Figure 10, I think.*

    This comment may arise due to the missing link between Fig. 10 and 11. and the requested frequency dependence is actually adressed by Fig. 10. Similarly to Fig. 11, we added now the KDE in Fig. 10 to show the data distribution. In the text, we link Fig. 10 and Fig. 11 better.

12. *P25:L32: Maybe not so intractable : Using an estimate of landslide width, and expectations on landslide scar aspect ratio (Domej et al., 2017) the scar area can be estimated and the crresponding high elevation pixels can be extracted within each polygons. This requires high quality mapping where individual landslides are not bundled together. But this approach has been validated and shown to improve correlation with rainfall in Marc et al., 2018a, and shown to improve volume nd erosion estimates in Marc et al., 2018b. This is a side topic for your study, but it could be mentionned, and at least this statement may be more nuanced.*

This comment highlights the landslide complexity and we changed the sentence.

Changes in text:

The reconstruction of the landslide failure planes is limited to statistical assessments of landslide inventories [Domej et al., 2017, Marc et al., 2019].

13. *Fig 12 : I would say the caption can be simple and clearer as : a) Aspect and hillslope inclination distribution within areas of the earthquake triggered landslides. This distribution is normalized by the distribution of the aspect of all hillslopes in the landslide affected area.*

    The formulation is less redundant and we changed it as stated.

14. *P21 L9 : This is an interesting and important point, but I would maybe rephrase it in terms of slopes. Because it is the slope that control the aspect of a landslide (that is what you measure on your DEM) and the earthquake is simply preferentially caussing failures in somes slopes (because wave motions and accelerations are stronger in some specific directions that will increase more or less the slope parallel component leading to failure). So the pattern of ground motion favor landslides in some part of the landscape, and at finer scale the directions of ground motions (FN/FP ratio) will force failure on specific slope aspects. I would say a a few lines discussing when and how different earthquakes will display strong directivity effect would be a good addition (maybe starting from your statement about Rupture speed and length ? Cf comment above).*

    We made changes and rephrased it in terms of slopes. As mentioned before, we investigated only one earthquake here. While the directivity effect is well studied and basically all major earhquakes display it, deriving generalizations (e.g. behaviour as function of rupture speed) with regard to interactions with landslide requires the investigation of more earthquake data. At this point, we could only speculate for the general case.

    Changes in text:

    This highlights that the earthquake affects the landslide locations (Fig. 6, 7); and will force failure on specific slopes facing in the direction of ground motion (Fig. 12, 14).

15. *P26 L18 : As commented above, Meunier 2007 (as well as Meunier 2013) consider landslide decay away from the source with a geometric and an exponential decay, similar to anelastic effect.*

    The highlighted sentence is formulated in an ambiguous way. It should read that Meunier et al. [2007]—as one of few—incorporates the attenuation term in landslide related GMMs.

    Change in text:

    The latter is commonly not incorporated in landslide studies but has been incorporated by more recent studies [e.g. Meunier et al., 2007, Massey et al., 2018].

References

Chi-Wen Chen, Hongey Chen, Lun-Wei Wei, Guan-Wei Lin, Tomoyuki Iida, and Ryuji Yamada. Evaluating the susceptibility of landslide landforms in Japan using slope stability analysis: a case study of the 2016 Kumamoto earthquake. *Landslides*, 14(5):1793–1801, oct 2017. ISSN 1612-510X. doi: 10.1007/s10346-017-0872-1. URL `http://link.springer.com/10.1007/s10346-017-0872-1`.

Prem P. Paudel, H. Omura, T. Kubota, and T. Inoue. Spatio-temporal patterns of historical shallow landslides in a volcanic area, Mt. Aso, Japan. *Geomorphology*, 88(1-2):21–33, jul 2007. ISSN 0169555X. doi: 10.1016/j.geomorph.2006.10.011. URL `http://linkinghub.elsevier.com/retrieve/pii/S0169555X0600465X`.

Prem P. Paudel, H. Omura, T. Kubota, and B. Devkota. Characterization of terrain surface and mechanisms of shallow landsliding in upper Kurokawa watershed, Mt Aso, western Japan. *Bulletin of Engineering Geology and the Environment*, 67(1):87–95, feb 2008. ISSN 1435-9529. doi: 10.1007/s10064-007-0108-z. URL `http://link.springer.com/10.1007/s10064-007-0108-z`.

Tatsuki Sato, Masahiro Chigira, and Yuki Matsushi. Topographic and Geological Features of Landslides Induced by the 2016 Kumamoto Earthquake in the Western Part of the Aso Caldera. *DPRI Annuals*, 60B:431–452, 2017. URL `http://hdl.handle.net/2433/229383`.

P. G. Somerville, N. F. Smith, R. W. Graves, and N. a. Abrahamson. Modification of Empirical Strong Ground Motion Attenuation Relations to Include the Amplitude and Duration Effects of Rupture Directivity. *Seismological Research Letters*, 68(1):199–222, 1997. ISSN 0895-0695. doi: 10.1785/gssrl.68.1.199.

By Paul Spudich, Brian S J Chiou, Robert Graves, Nancy Collins, and Paul Somerville. A Formulation of Directivity for Earthquake Sources Using Isochrone Theory. *U.S. Geol. Surv. Open-File Rept. 2004-1268*, page 54, 2004.

P. Spudich, J.R. Bayless, J. Baker, Brian S J Chiou, B. Rowshandel, S. Shahi, and Paul Somerville. Final Report of the NGA-West2 Directivity Working Group. Technical Report Final, Pacific Earthquake Engineering Research Center, 2013.

Kun Song, Fawu Wang, Zili Dai, Akinori Iio, Osamu Osaka, and Seiji Sakata. Geological characteristics of landslides triggered by the 2016 Kumamoto earthquake in Mt. Aso volcano, Japan. *Bulletin of Engineering Geology and the Environment*, pages 1–10, jun 2017. ISSN 1435-9529. doi: 10.1007/s10064-017-1097-1. URL `http://link.springer.com/10.1007/s10064-017-1097-1`.

Ching Hung, Guan-Wei Lin, Huei-Sian Syu, Chi-Wen Chen, and Hsin-Yi Yen. Analysis of the Aso-Bridge landslide during the 2016 Kumamoto earthquakes in Japan. *Bulletin of Engineering Geology and the Environment*, (200): 1–11, jul 2017. ISSN 1435-9529. doi: 10.1007/s10064-017-1103-7. URL `http://link.springer.com/10.1007/s10064-017-1103-7`.

Tolga Gorum, Xuanmei Fan, Cees J. van Westen, Run Qiu Huang, Qiang Xu, Chuan Tang, and Gonghui Wang. Distribution pattern of earthquake-induced landslides triggered by the 12 May 2008 Wenchuan earthquake. *Geomorphology*, 133(3-4):152–167, 2011. ISSN 0169555X. doi: 10.1016/j.geomorph.2010.12.030. URL `http://dx.doi.org/10.1016/j.geomorph.2010.12.030`.

Khang Dang, Kyoji Sassa, Hiroshi Fukuoka, Naoki Sakai, Yuji Sato, Kaoru Takara, Lam Huu Quang, Doan Huy Loi, Pham Van Tien, and Nguyen Duc Ha. Mechanism of two rapid and long-runout landslides in the 16 April 2016 Kumamoto earthquake using a ring-shear apparatus and computer simulation (LS-RAPID). *Landslides*, 13 (6):1525–1534, dec 2016. ISSN 1612-510X. doi: 10.1007/s10346-016-0748-9. URL `http://dx.doi.org/10.1007/s10346-016-0748-9` `http://link.springer.com/10.1007/s10346-016-0748-9`.

Edwin L Harp and Raymond C Wilson. Shaking Intensity Thresholds for Rock Falls and Slides : Evidence from 1987 Whittier Narrows and Superstition Hills Earthquake Strong-Motion Records. *Bulletin of the Seismological Society of America*, 85(6):1739–1757, 1995.

Niels Hovius and Patrick Meunier. Earthquake ground motion and patterns of seismically induced landsliding. In John J. Clague and Douglas Stead, editors, *Landslides*, pages 24–36. Cambridge University Press, Cambridge, 2012. doi: 10.1017/CBO9780511740367.004. URL `https://www.cambridge.org/core/product/identifier/9780511740367%23c00206-3-1/type/book`.

Marco Massa, Simone Barani, and Sara Lovati. Overview of topographic effects based on experimental observations: meaning, causes and possible interpretations. *Geophysical Journal International*, 197(3): 1537–1550, jun 2014. ISSN 0956-540X. doi: 10.1093/gji/ggt341. URL `https://academic.oup.com/gji/article-lookup/doi/10.1093/gji/ggt341`.

Steven L Kramer. Geotechnical earthquake engineering. In prentice–Hall international series in civil engineering and engineering mechanics. *Prentice-Hall, New Jersey*, 1996.

Paul Spudich and Brian S J Chiou. Directivity in NGA earthquake ground motions: Analysis using isochrone theory. *Earthquake Spectra*, 24(1):279–298, 2008. ISSN 87552930. doi: 10.1193/1.2928225.

G Domej, C Bourdeau, L Lenti, S Martino, and K Pluta. Mean landslide geometries inferred from globla database. *94 Italian Journal of Engineering*

Geology and Environment, 2:87–107, 2017. doi: 10.4408/IJEGE.2017-02.O-05.

Odin Marc, Robert Behling, Christoff Andermann, Jens M Turowski, Luc Illien, Sigrid Roessner, and Niels Hovius. Long-term erosion of the Nepal Himalayas by bedrock landsliding: the role of monsoons, earthquakes and giant landslides. *Earth Surface Dynamics*, 7(1):107–128, jan 2019. ISSN 2196-632X. doi: 10.5194/esurf-7-107-2019. URL https://www.earth-surf-dynam.net/7/107/2019/.

Patrick Meunier, Niels Hovius, and A. John Haines. Regional patterns of earthquake-triggered landslides and their relation to ground motion. *Geophysical Research Letters*, 34(20):1–5, 2007. ISSN 00948276. doi: 10.1029/2007GL031337.

C. Massey, D. Townsend, E. Rathje, K. E. Allstadt, B. Lukovic, Y. Kaneko, B. Bradley, J. Wartman, R. W. Jibson, D. N. Petley, N. Horspool, I. Hamling, J. Carey, S. Cox, J. Davidson, S. Dellow, J. W. Godt, C. Holden, K. Jones, A. Kaiser, M. Little, B. Lyndsell, S. McColl, R. Morgenstern, F. K. Rengers, D. Rhoades, B. Rosser, D. Strong, C. Singeisen, and M. Villeneuve. Landslides Triggered by the 14 November 2016 Mw 7.8 Kaikoura Earthquake, New Zealand. *Bulletin of the Seismological Society of America*, 108(3B):1630–1648, jul 2018. ISSN 0037-1106. doi: 10.1785/0120170305. URL https://pubs.geoscienceworld.org/ssa/bssa/article/529881/Landslides-Triggered-by-the-14
https://pubs.geoscienceworld.org/ssa/bssa/article/108/3B/1630/529881/Landslides-Trigger

Effects of finite source rupture on landslide triggering: The 2016 M_W 7.1 Kumamoto earthquake

Sebastian von Specht[1,2], Ugur Ozturk[1,3,4], Georg Veh[3], Fabrice Cotton[1,2], and Oliver Korup[2,3]

[1]Helmholtz Centre Potsdam - GFZ German Research Centre for Geosciences, Telegrafenberg, 14473 Potsdam, Germany
[2]University of Potsdam, Institute of Geosciences, Karl-Liebknecht-Str. 24-25, 14476 Potsdam-Golm, Germany
[3]University of Potsdam, Institute of Environmental Science and Geography, Karl-Liebknecht-Str. 24-25, 14476 Potsdam-Golm, Germany
[4]Potsdam Institute for Climate Impact Research (PIK) e. V., Telegrafenberg, 14473 Potsdam, Germany

Correspondence: Sebastian von Specht (sspecht@uni-potsdam.de)

Abstract. The propagation of a seismic rupture on a fault introduces spatial variations in the seismic wavefield surrounding the fault. This directivity effect results in larger shaking amplitudes in the rupture propagation direction. Its seismic radiation pattern also causes amplitude variations between the strike-normal and strike-parallel components of horizontal ground motion. We investigated the landslide response to these effects during the 2016 Kumamoto earthquake (M_W7.1) in central Kyushu (Japan). Although the distribution of some 1,500 earthquake-triggered landslides as function of rupture distance is consistent with the observed Arias intensity, the landslides were more concentrated to the northeast of the southwest-northeast striking rupture. We examined several landslide susceptibility factors: hillslope inclination, median amplification factor (MAF) of ground shaking, lithology, land cover, and topographic wetness. None of these factors sufficiently explains the landslide distribution or orientation (aspect), although the landslide headscarps have an elevated hillslope inclination and MAF. We propose a new physics-based ground motion model that accounts for the seismic rupture effects, and demonstrate that the low-frequency seismic radiation pattern is consistent with the overall landslide distribution. Its spatial pattern is influenced by the rupture directivity effect, whereas landslide aspect is influenced by amplitude variations between the fault-normal and fault-parallel motion at frequencies < 2 Hz. This azimuth-dependence implies that comparable landslide concentrations can occur at different distances from the rupture. This quantitative link between the prevalent landslide aspect and the low-frequency seismic radiation pattern can improve coseismic landslide hazard assessment.

1 Introduction

Landslides are one of the most obvious and hazardous consequences of earthquakes. Acceleration of seismic waves alters the force balance in hillslopes and temporarily exceeds shear strength (Newmark, 1965; Dang et al., 2016). Greatly increased landslide rates have been reported on hillslopes close to earthquake rupture, mostly tied to ground acceleration (Gorum et al., 2011) and lithology (Chigira and Yagi, 2006). Substantial geomorphological and seismological data sets are required to assess the response of landslides to ground motion and a growing number of studies has shed light on the underlying links (e.g. Lee, 2013; Allstadt et al., 2018; Roback et al., 2018; Fan et al., 2018). Several seismic measures such as vertical and horizontal peak

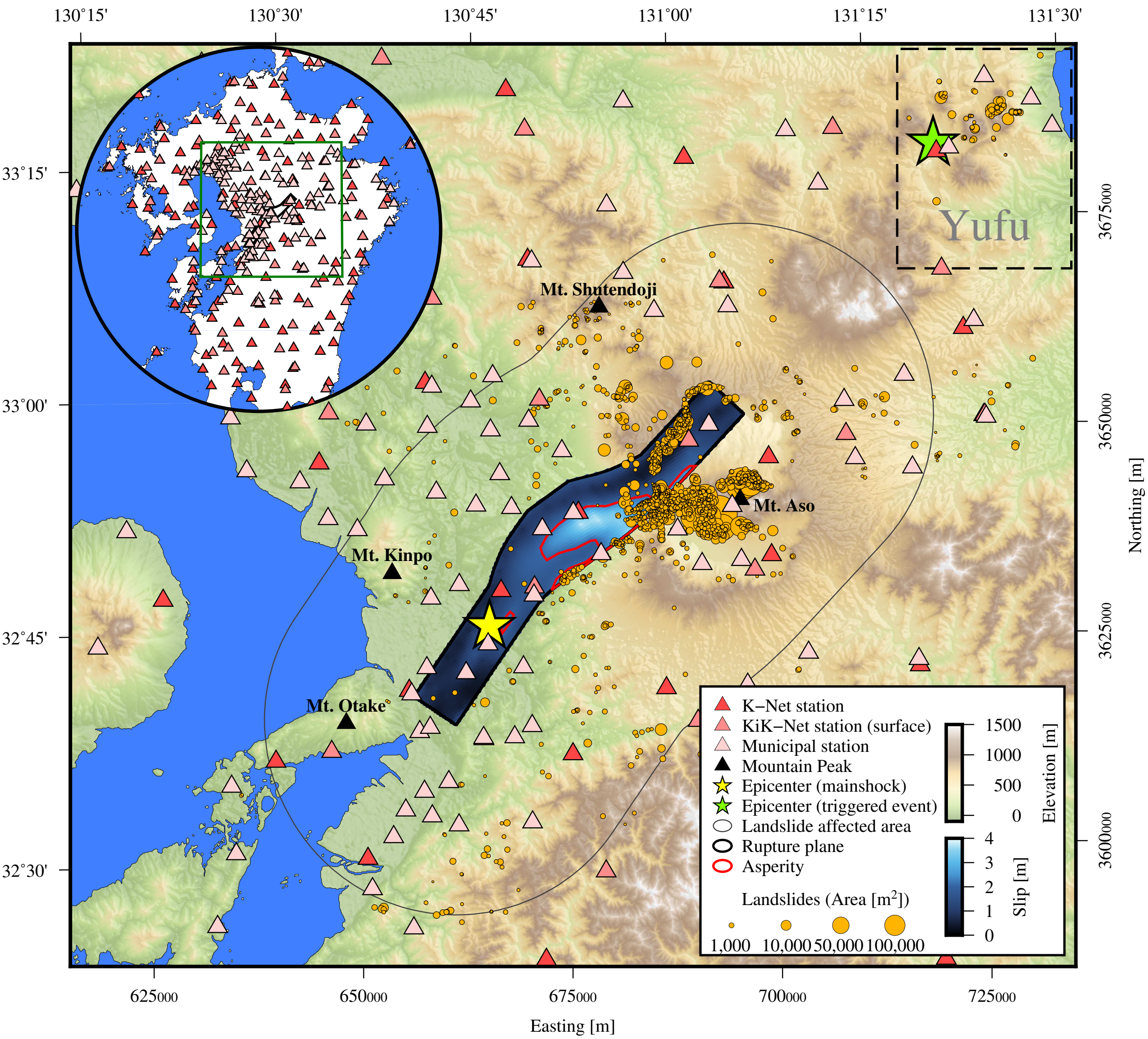

Figure 1. The area of Kyushu affected by coseismic landslides triggered by the 2016 M_W 7.1 Kumamoto earthquake. The colored patch is the slip distribution of the rupture model by Kubo et al. (2016), the dashed box encompasses landslides related to the triggered event in Yufu (epicenter location after Uchide et al. (2016)). The inset map shows the station network within 150 km of the rupture.

ground acceleration (PGA) (Miles and Keefer, 2009), root-mean square (RMS) acceleration or Arias intensity (I_A) (Arias, 1970; Keefer, 1984; Harp and Wilson, 1995; Jibson et al., 2000; Jibson, 2007; Torgoev and Havenith, 2016), seismic source-moment release, hypocentral depth, as well as rupture extent and propagation (Newmark, 1965) correlate with landslide density (Meunier et al., 2007).

Landslides concentrate in the area of strongest ground acceleration (Meunier et al., 2007), whereas total landslide area decreases from the earthquake rupture with the attenuation of peak ground acceleration (Dadson et al., 2004; Taylor et al., 1986). This general pattern is modified by morphometrics (e.g. local hillslope inclination, curvature) and geological parameters (e.g. lithology, geological structure, land cover) (Gorum et al., 2011; Havenith et al., 2015) that influence landslide susceptibility (Pawluszek and Borkowski, 2017) on top of seismic amplification (Maufroy et al., 2015). For instance, Tang et al. (2018) found that lithology, PGA, and distance from the rupture plane are important in assessing the distribution of landslides triggered by the 2008 Wenchuan earthquake (M_W 7.9). Fan et al. (2018) found that hillslope aspect and slope were important determinants of the landslide distribution resulting from the 2017 Jiuzhaigou earthquake (M_W 6.5).

On April 16, 2016 at 16:25 UTC central Kyushu was hit by a M_W 7.1 earthquake (Fig. 1). The left-lateral dip-slip event ruptured along the Futagawa and Hinagu faults striking NW-SE with a hypocentral depth of 11 km (e.g. Kubo et al., 2016). The rupture propagated northeastward and stopped at Mt. Aso. Fault source inversions show a northeast propagation of the rupture originating under Kumamoto city with highest slip near the surface at the western rim of the Aso caldera (e.g. Kubo et al., 2016; Asano and Iwata, 2016; Moore et al., 2017; Uchide et al., 2016; Yagi et al., 2016; Yoshida et al., 2017). The earthquake triggered approximately 1,500 landslides (National Research Institute for Earth Science and Disaster Prevention, 2016) that concentrated mainly inside the caldera and the flanks of Mt. Aso on the Pleistocene and Holocene lava flow deposits (Paudel et al., 2008; Sidle and Chigira, 2004), although most of the terrain near the earthquake rupture is rugged (Fig. 1). Thus, we hypothesize that rupture directivity causes an asymmetric distribution of landslides around the rupture plane, because of more severe ground motion along the propagating rupture (Somerville et al., 1997; Hovius and Meunier, 2012). Similarly asymmetric landslide distributions attributed to rupture directivity were repoprted for the 2002 Denali earthquake (M_W 7.9) (Frankel, 2004; Gorum et al., 2014), and the 2015 Gorkha earthquake (M_W 7.8) (Roback et al., 2018). In case of the 1999 Chi-Chi earthquake, Lee (2013) speculated that the prevalent landslide aspects were correlated to the fault movement direction (Ji et al., 2003; Meunier et al., 2008). These observations indicate that the rupture process introduces variations on the incoming energy on hillslopes.

Here we link those dominant near-surface seismic characteristics relevant to the pattern and orientation of coseismic landslides. We investigate the geological conditions (lithology, aspect, hillslope inclination, topographic amplification, soil wetness) in central Kyushu as well as seismic waveform records from 240 seismic stations within 150 km of the rupture (Fig. 1). The two most prominent seismic effects—well founded in seismological theory (e.g. Aki and Richards, 2002) and documented in empirical relationships (e.g. Somerville et al., 1997)—are the rupture directivity and amplitude variations of fault-normal and fault-parallel motion. We examine whether the geomorphic characteristics around the Aso caldera made this area more susceptible to landslides than the surrounding topography near the earthquake rupture; or whether rupture effects control the asymmetric distribution of the landslides. We introduce a ground motion metric related to azimuth-dependent seismic energy (i.e. seismic velocity), because these effects attenuate with increasing frequency and are less captured by acceleration based metrics. We conclude by proposing a new ground-motion model that is consistent with the observed coeseismic landslide pattern.

2 Data

We combine data sets on the response of landslides to the earthquake, including topography, land cover, geology, seismic waveforms, velocity structure, near surface characteristics, and landslide location and planform (Fig .2).

2.1 Topographic data

Most topographic data used in this study are provided by the Japan Aerospace Exploration Agency (JAXA) and its Advanced Land Observing Satellite (ALOS) project with a horizontal resolution of 1" ($\approx$ 30 m). This digital surface model (DSM) forms the basis for computing aspect, hillslope inclination, the median amplification factor (MAF, Maufroy et al., 2015), and the topographic wetness index (Böhner and Selige, 2006). The ALOS project also provides data on land cover including anthropogenic influence (sealing, agriculture) and vegetation. While data on major geological units are from the Seamless Digital Geological Map of Japan (scale 1:200,000) by the Geological Survey of Japan.

2.2 Topographic amplification of ground motion

Topographic features, such as mountains and valleys, can amplify or attenuate seismic waves (Massa et al., 2014; Maufroy et al., 2012, 2015). Largest ground-motion variations occur on hillslopes and summits, whereas variations are intermediate on narrow ridges, and low on valley floors. Maufroy et al. (2015) introduced proxies for these topographic site effects, of which we use the median amplification factor (MAF), based on the topographic curvature, and the S-wave velocity v_S traveling at frequency f:

$$MAF(f) = 8 \times 10^{-4} \frac{v_S}{f} C_S\left(\frac{v_S}{2f}\right) + 1 \quad (1)$$

where $C_S\left(\frac{v_S}{2f}\right)$ is the topographic curvature convolved with a normalized smoothing kernel based on two 2D box-car functions as a function of v_S and f.

The curvature is estimated from the DSM (Zevenbergen and Thorne, 1987; Maufroy et al., 2015) and the seismic velocity v_S is the average S-wave velocity of the uppermost 500 m from the model by Koketsu et al. (2012).

Another site effect that influences landslide potential is the local soil or groundwater content, which can be modeled for uniform conditions to first order using the topographic wetness index (TWI) of Böhner and Selige (2006):

$$TWI = \log \frac{A_c}{\tan\beta}, \quad (2)$$

where A_c is the upslope catchment area and β is the hillslope inclination derived from the DSM with filled sinks (Planchon and Darboux, 2001).

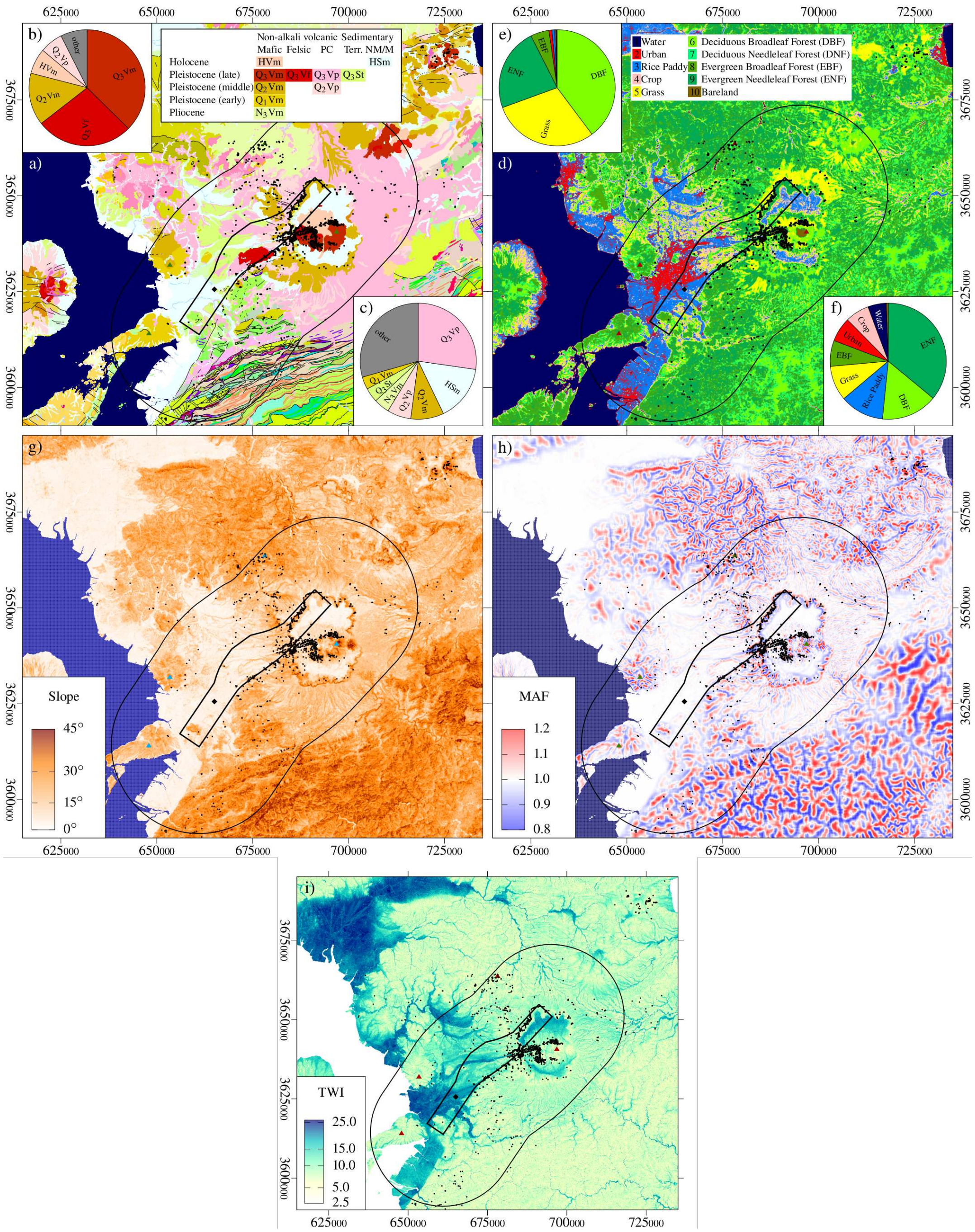

Figure 2. a) Geology of central Kyushu. The most common geological units of the landslides (black dots) are shown in b). For the landslide affected area (outer black line) the dominant geological units are in c). The inner black line denotes the rupture area, containing the hypocenter (black diamond). d) Land cover. Land cover in the landslide areas is shown in e) and for the the entire landslide affected area in f). g) Hillslope inclination. h) Median amplification factor (MAF). i) Topographic Wetness Index (TWI).

2.3 Ground motion data

Ground-motion data are from the Kik-Net/K-Net of the National Research Institute for Earth Science and Disaster Prevention (NIED) of Japan. NIED operates for Kik-Net both borehole and surface stations, and we use the latter only. The Japan Meteorological Agency (JMA) also released seismic data from the municipal seismic network for the largest earthquakes of the Kumamoto sequence. In total, data from 240 stations in Kyushu are available with complete azimuthal coverage within 150 km from the earthquake rupture (Fig. 1).

The analysis of seismic waveforms is based on accelerometric data only. Both the NIED and JMA data are unprocessed and we follow the strong motion processing guidelines by Boore and Bommer (2005). We use both acceleration and velocity in further processing, and integrate the accelerograms to obtain velocity records. We correct the data with the automated baseline correction routine by Wang et al. (2011). The JMA accelerometric data further require a piece-wise baseline correction prior to the displacement baseline correction due to abrupt (possibly instrument related) jumps (Boore and Bommer, 2005; Yamada et al., 2007). We use the automated correction for baseline jumps by von Specht, 2018 (in prep.).

An earthquake was triggered approximatley 80 km to the northeast in Yufu 32 s after the Kumamoto earthquake (Uchide et al., 2016) (Fig. 1). Due to the close succession of the two events, waveforms of the triggered event interfere with the coda of the Kumamoto earthquake. We taper the data to reduce signal contributions by the triggered event. The taper position is based on theoretical traveltime differences between the P wave ($v_P = 5700$ m s^{-1}) arrival of the Kumamoto earthquake and the S wave arrival ($v_S = 3300$ m s^{-1}) of the triggered event. The respective travel paths to the stations are measured from the hypocenters. Since fewer instruments are located to the northeast and the triggered event close to the sea, less than 10% of the data are strongly contaminated by the triggered event.

NIED hosts the rupture plane model of Kubo et al. (2016), which describes the slip history on a curved rupture plane (based on the surface traces of the Futagawa and Hinagu faults) with a total length of 53.5 km and width of 24.0 km (Fig. 1). We use the extent and shape of the rupture plane to estimate the landslide affected area and to define the rupture plane distance r_{rup}, the shortest distance from the rupture plane. We follow the approach of Somerville et al. (1999) to identify the asperity from the rupture plane model, which is is the area with more than 1.5 times the average slip.

The underground structure in terms of seismic velocities (v_P, v_S) and density (ρ) (Koketsu et al., 2012) are available for 23 layers down to the mantle in ≈ 0.1 degree resolution covering all of Japan; we only consider the layers of the upper 0.5 km to compute a velocity average for and the MAF.

NIED provides data for the subsurface shear wave velocities (v_{S30}) as well as site amplifications factors S_{amp}. Contrary to v_S by Koketsu et al. (2012), v_{S30} is derived for the upper 30 m only and more suitable for energy estimates, which requires velocities at the surface (recording station). The site amplification factor S_{amp} describes by how much seismic waves are amplified independent of their frequency.

2.4 Landslide data

Detailed landslide data are provided by NIED as polygons (Fig. 1), mapped from aerial imagery with sub-meter resolution at different times after the Kumamoto earthquake. The first data set contains landslides that were identified between April 16 to 20, though the area close to the summit of Mt. Aso was not covered. A second data set was collected on April 29, 2016 and covers those parts of Mt. Aso that remained unmapped. However, the second data set may contain rainfall induced landslides, since the rainy season in Kyushu starts in May (Matsumoto, 1989), and there was rainfall after the Kumamoto earthquake and landslides triggered by volcanic activity. We selectively combine the two data sets for this study, using only those landslides from the second database, that are also partly present in the first data set. We exclude any rainfall triggered landslides with this approach, though possibly omitting seismically induced landslides exclusive to the second database. However, the area in question is comparatively small to the full extent of the study area, and the missing landslides are minor in terms of their area.

Several landslides cluster ≈ 80 km to the northeast of the mainshock in the municipalities Yufu and Beppu (Fig. 1), that were hit by a triggered earthquake (Uchide et al., 2016). We hypothesize that the distant northeastern landslides were induced by this triggered event. This also explains the considerable gap of landslides (≈ 50 km) between Yufu and Aso (Fig. 1) in otherwise steep topography. Hence we exclude the landslides near Yufu and Beppu ($<$10% of all landslides, $<$3% of total landslide area) from our database.

Apart from the special release of landslide data for the 2016 Kumamoto Earthquake, NIED hosts a landslide database for all Japan (National Research Institute for Earth Science and Disaster Prevention, 2014). This database covers unspecified landslides of any origin. We extract a subset from this landslide database to compare it with the landslides triggered by the Kumamoto earthquake. Contrary to the special Kumamoto release, only the landslide deposits are mapped as polygons, whereas the scarps are mapped as lines. We manually define polygons representing the total landslide area bound by the scarp line and covering the deposit area to make both data sets comparable and because the landslide source area is generally not identical with the deposit area.

3 Total area affected by landsliding

We define the landslide affected area, in which coseismic landsliding occurred, as the area spanned by the rupture plane distance covering 97.5 % of the total landslide area (Harp and Wilson, 1995; Marc et al., 2017). Thus the total landslide affected area is 3968.6 km^2 and within 22.9 km distance from the rupture plane.

An M_W 7.1 event with a fault length of 53.5 km and an asperity length of 12.78 km (3 km) results in a landslide affected area of 3914 km^2 (4406 km^2) using parameters proposed by Marc et al. (2016). We derived the event depth of 11.1 km as the moment weighted average of the rupture model of Kubo et al. (2016). Both estimates are consistent with our area estimate. Marc et al. (2016) introduced a topographic constant, A_{topo}, relating the total landslide area to the area that excludes basins and inundated areas. We estimate A_{topo} from the ALOS land cover finding that 97 % of all landslides occurred in areas without anthropogenic influence, i.e. land with urban and agricultural use, and water bodies. We exclude water bodies, urban areas—

predominantly the metropolitan area of Kumamoto City, and rice paddies from the topographic analysis, obtaining an affected area of 3037 km^2, i.e. $A_{topo} = 0.68$.

4 Total landslide area

Total landslide area is linked to several earthquake parameters, mostly magnitude and hypocenter or average rupture-plane depth (Keefer, 1984; Marc et al., 2016). We adopted the relation by Marc et al. (2016) to check for completeness of the total landslide area of 6.38 km^2. The actual total landslide failure plane is likely smaller, as the NIED data set provides the combined area of depletion and accumulation. The modal hillslope inclination is estimated at 15°. Instead of the earthquake magnitude scaling relation (Leonard, 2010) used by Marc et al. (2016), we use the rupture extent reported by Kubo et al. (2016). The area model requires the average length of the seismic asperities, which Marc et al. (2016) globally assumed as 3 km. However, Somerville et al. (1999) derived a relationship of asperity sizes based on seismic moment that results in an average asperity length of 12.78 km for the 2016 Kumamoto Earthquake. This length is consistent with the asperity sizes found by Yoshida et al. (2017) for their finite rupture model. The estimated landslide area with an asperity length of 3 km results in a predicted total landslide area of 12.90 km^2, while with the magnitude scaled asperity size of Somerville et al. (1999) the landslide area is 3.03 km^2. The landslide area estimates with constant asperity length and moment dependent asperity length differ by a factor of 2 and 0.5 from the NIED data set, respectively.

Landslide concentration is defined as landslide area per area at a given distance band (Meunier et al., 2007). For the seismic processing, we consider the rupture plane distance r_{rup} based on the rupture model, instead of the hypocentral distance (Meunier et al., 2007) or the Joyner-Boore distance (Harp and Wilson, 1995).

5 Ground motion & seismically induced landsliding

5.1 Coseismic landslide displacement

The sliding-block model of Newmark (1965) is widely used to estimate coseismic hillslope performance (e.g. Kramer, 1996; Jibson, 1993, 2007). The model estimates the permanent displacement on a hillslope affected by ground motion. Newmark (1965) established a relation for hillslope displacement in terms of the maximum velocity at the hillslope for a single rectangular pulse, v_{max} $\left[\mathrm{m\,s^{-1}}\right]$

$$d_s = \frac{v_{max}^2}{2}\left(\frac{1}{Aa_y} - \frac{1}{A}\right) \tag{3}$$

where A is the magnitude of the acceleration pulse and a_y $\left[\mathrm{m\,s^{-2}}\right]$ the yield acceleration, which is the minimum pseudostatic acceleration required to produce instability. For downslope motion along a sliding plane, a_y is related to the angle of internal friction, ϕ_f and the hillslope inclination, δ, by

$$a_y = g\left(\frac{\tan\phi}{\tan\delta}\right)\sin\delta = g(\overline{FS} - 1)\sin\delta \tag{4}$$

with the average factor of safety $\overline{FS}$. Chen et al. (2017) characterized unstable hillslopes—related to both rainfall and earthquakes—by a safety factor of $FS < 1.5$.

An upper bound for the displacement d_s, is based on two ground motion parameters (Newmark, 1965; Kramer, 1996):

$$d_{max} = \frac{PGA}{a_y}\frac{PGV^2}{a_y}, \tag{5}$$

where PGA $\left[\mathrm{m\,s^{-2}}\right]$ and PGV $\left[\mathrm{m\,s^{-1}}\right]$ are the peak ground acceleration and velocity, respectively. Thus, the coseismic hillslope performance can be characterized by velocity and acceleration. In the following sections, we derive a ground-motion model based on the acceleration-related Arias intensity and the velocity-related radiated seismic energy.

5.2 Ground motion metrics

Though PGA is the most widely used ground-motion metric in geotechnical engineering, the Arias intensity I_A (Arias, 1970) is widely used to characterize strong ground motion for landslides:

$$I_A = \frac{\pi}{2g}\int\limits_{T_1}^{T_2} a(t)^2 dt, \tag{6}$$

where $g = 9.80665\ \mathrm{m\,s^{-2}}$ is standard gravity and T_1 and T_2 are the times where strong ground motion starts and cedes. The acceleration $a(t)$ has units of $\mathrm{m\,s^{-2}}$ and the Arias intensity has units $\mathrm{m\,s^{-1}}$. The Arias intensity captures both the duration and amplitude of strong motion. Empirical relationships between I_A and d_s in terms of earthquake magnitude and epicenter distance have been developed (e.g. Jibson, 1993; Bray and Travasarou, 2007; Jibson, 2007).

Since PGA and I_A are related to each other (e.g. Romeo, 2000) and the hillslope displacement depends on both velocity and acceleration (Eq. (3), (5)), it is reasonable to characterize velocity similar to Arias intensity. The velocity counterpart to I_A is $IV2$, the integrated squared velocity (Kanamori et al., 1993; Festa et al., 2008):

$$IV2 = \int\limits_{T_1}^{T_2} v(t)^2 dt \tag{7}$$

The squared velocity is also used in radiated seismic energy estimates. The quantity j_E is the radiated energy flux of an earthquake and estimated by (Choy and Cormier, 1986; Kanamori et al., 1993; Newman and Okal, 1998)

$$j_E = \frac{\rho c}{S_{amp}^2} e^{-k r_{rup}} IV2 \tag{8}$$

where ρ and c are the density and seismic wave velocity at the recording site and S_{amp} is the site specific amplification factor. The distance from the rupture is given by r_{rup} and k is a term for path attenuation (Anderson and Richards, 1975), and effects of transmission and reflection (Kanamori et al., 1993). The attenuation constant k is also influenced by anisotropy and structure heterogeneity (Campillo and Plantet, 1991; Bora et al., 2015). The full definition of the energy flux includes two terms for compressional waves ($c = v_P$) and shear waves ($c = v_S$). The radiated energy of an earthquake, E_S, results from the integral over the wavefront surface

$$E_S = \iint j_E dA, \tag{9}$$

where A is the area of the surface through which the wave passes at the recording station and represents the geometrical spreading.

The radiated seismic energy E_S describes the energy leaving the rupture area and is related to the seismic moment (Hanks and Kanamori, 1979)

$$E_S = \frac{\Delta\sigma}{2\mu} M_0, \tag{10}$$

where $\Delta\sigma$ is the stress drop, μ the shear modulus, and M_0 the seismic moment. We make use of this relation, when considering the magnitude related term in the ground motion model. Since most seismic energy is released as shear waves, we apply the shear wave velocity at the recording site (v_S) to the entire waveform, i.e. we assume that all waves arrive with velocity v_S at a site. This assumption has the advantage that it does not require a separation of the record into P- and S-waveforms, simplifying the computation. In appendix B we show from a theoretical perspective that using a uniform v_S has only a small impact on the overall energy estimate. The site-specific correction term for the energy estimate $\hat{E}$, based on Eq. (8) and (9) becomes

$$\hat{E} = \frac{\hat{A}\rho v_S}{S_{amp}^2} e^{-kr_{rup}} IV2 \tag{11}$$

While E_S is the radiated seismic energy at the source, $\hat{E}$ is estimated from the velocity records at a station and only approximates E_S. Therefore, $\hat{E}$ may differ from the true and unknown radiated energy E_S (Kanamori et al., 1993). Several assumptions characterize $\hat{E}$

- All energy is radiated as S-waves in an isotropic, homogeneous medium
- Geometrical spreading is corrected for an isotropic, homogeneous medium
- Since $IV2$ (Eq. (7)) depends on the radiation pattern, $\hat{E}$ depends on azimuth
- Attenuation is homogeneous
- Surface waves are not considered
- Site amplification is frequency-independent

Below, we investigate the azimuthal variation of the energy estimates to characterize the radiation pattern.

The estimated wavefront area $\hat{A}$ is related to the rupture extent and r_{rup}, and $\hat{A}$ corresponds to a simplified version of the wave front area approximation by Schnabel and Bolton Seed (1973); Shoja-taheri and Anderson (1988):

$$\hat{A} = 2WL + \pi r_{rup}(L + 2W) + 2\pi r_{rup}^2 \tag{12}$$

The extent of the rupture is assumed to be rectangular with length L and width W. Equation (12) describes a cuboid with rounded corners with only half of its surface considered, because no energy flux is assumed to be transmitted above ground.

While the geometrical spreading correction is expressed analytically as the wavefront area $\hat{A}$, we estimate the attenuation parameter k. Attenuation changes with distance as a power law at short distances (< 150 km) (Anderson and Richards, 1975) and longer distances are not considered. An empirical attenuation relationship is:

$$\ln Y = C + k r_{rup}, \tag{13}$$

where Y is

$$Y = \frac{\hat{A}\rho v_S}{S_{amp}^2} \int\limits_{T_1}^{T_2} IV2, \tag{14}$$

i.e. the logarithm of the energy estimate without the attenuation term $e^{-kr_{rup}}$ from Eq. (11). The dummy variable C is only used for estimating k and not in the final correction for attenuation. A distance independent form of the Arias intensity, i.e. corrected for geometrical spreading and attenuation, is defined by

$$I_{A,A} = \frac{\hat{A}}{S_{amp}^2} e^{-kr_{rup}} I_A, \tag{15}$$

where k is determined by Eq. (13) and setting $Y = I_A \hat{A}$. The corrected Arias intensity $I_{A,A}$ is the acceleration based counterpart to $\hat{E}$.

Low-frequency effects, like directivity, are better captured with a velocity based metric (e.g. azimuth-dependent energy estimate), than an acceleration based metric (Arias intensity) alone.

In terms of the Fourier transform, the sensitivity of acceleration at higher frequencies becomes apparent, as the Fourier transform of the time derivative of any function is

$$\mathcal{F}(\dot{f}(t)) = i\omega \mathcal{F}(f(t)) \tag{16}$$

and thus scales with frequency in the spectrum. The frequency sensitivity of $IV2$ and I_A is related to the squared spectrum given the the metrics. As an example, we show in Fig. 3 the different spectral sensitivities of $IV2$ and I_A for a theoretical seismic source spectrum (Brune, 1970). $IV2$, and thus $\hat{E}$ has a higher sensitivity to lower frequencies than I_A. The low-frequency part of the spectrum can be accounted for by considering $IV2$ in a ground-motion model.

5.3 Landslide related ground-motion models

The basic form of landslide related ground motion models for Arias intensity is based on earthquake magnitude M and distance from the earthquake rupture r (e.g. Harp and Wilson, 1995).

$$\ln I_A = p_1 + p_2 M + p_3 \ln r \tag{17}$$

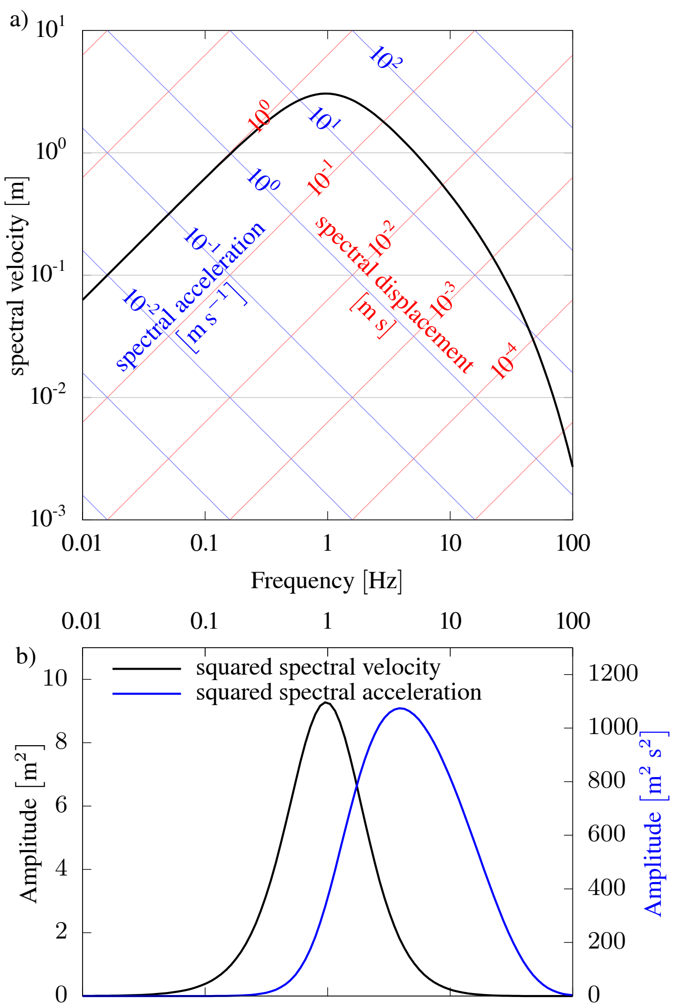

Figure 3. a) Far-field spectrum after Brune (1970). The spectrum can be read as displacement (red), velocity (black) and acceleration (blue). b) The squared Brune spectrum corresponds to the frequency sensitivity of velocity based $IV2$ (blue) and the acceleration based I_A (black).

This form is widely used (Keefer, 1984; Harp and Wilson, 1995). In engineering seismology, ground motion models usually have an additional distance term for anelastic attenuation

$$\ln I_A = c_1 + c_2 M + c_3 r + (c_4 + c_5 M)\ln r \tag{18}$$

This is a modified version of the model template by Kramer (1996). While Eq. 17 and Eq. 18 share some parameters (p_1, c_1 and p_2, c_2), the geometric spreading term includes not only distance dependence (p_3, c_4) but also has a magnitude dependent component (c_5). In addition, anelastic attenuation is included as well (related to c_3) in Eq. 18. The template of Kramer (1996) relates to the majority of GMPEs in engineering seismology. Models of this kind address strong motion in the context of landsliding (Travasarou et al., 2003; Bray and Rodriguez-Marek, 2004). The incorporation of anelastic attenuation is less common in landsliding GMMs and not mentioned in these studies but included in more recent studies (Meunier et al., 2007, 2013; Yuan et al., 2013).

We exchange the magnitude term from Eq. (18) with a site-dependent energy term, assuming that landsliding is more related to the energy of incoming seismic waves than to the moment at the source. We replace moment magnitude by the logarithm of energy (Eq. (11)), since energy is proportional to the seismic moment M_0 (Eq. (10)). Based on the site-dependent energy estimate $\hat{E}$, we propose the model

$$\ln I_A = c_1 + c_2 \ln \hat{E} + c_3 r + (c_4 + c_5 \ln \hat{E})\ln r \tag{19}$$

The five coefficients are inferred by non-linear least squares (e.g. Tarantola, 2005). We use the rupture plane distance (r_{rup}), i.e. the shortest distance between a site and the rupture plane.

5.4 Rupture directivity model

In the NGA-west2 guidelines (Spudich et al., 2013), the directivity effect is modeled by isochrone theory (Bernard and Madariaga, 1984; Spudich and Chiou, 2008) or the azimuth between epicenter and site (Somerville et al., 1997). We use the latter approach and model directivity for estimated energy and corrected Arias intensity in a simplified way:

$$\ln \hat{E}_\theta = \ln \hat{E}_0 + a_E \cos(\theta - \theta_E) \tag{20}$$

$$\ln I_{A,A,\theta} = \ln I_{A,A,0} + a_I \cos(\theta - \theta_I), \tag{21}$$

where $\hat{E}_0$ and $I_{A,A,0}$ are the offset (average), a_E and a_I the amplitude of variation with azimuth and θ_E and θ_I are the azimuths of the maximum. The definition of θ is similar to that of Somerville et al. (1997) as the angle measured between the epicenter and the recording site with the difference of being measured clockwise from north. The azimuths of the maximum, θ_E and θ_I, are free parameters because (1) the rupture is assumed to have occurred on two faults and has thus variable strike, and (2) the event is not pure strike-slip and has a normal faulting component. We therefore do not expect a match between the rupture strike and θ_E and θ_I. The geometrical spreading is already incorporated in the energy estimate as a distance term (Somerville et al., 1997; Spudich et al., 2013).

5.5 Model for fault-normal to fault-parallel ratio

The ratio of the response spectra of the horizontal sensor components is a function of oscillatory frequency f_{osc}.

The north and east components (E, N) of the sensor are rotated to be fault-normal (FN) and fault-parallel (FP).

$$FN = E\cos\phi - N\sin\phi \tag{22}$$

$$FP = E\sin\phi + N\cos\phi \tag{23}$$

$$FN/FP = \frac{SA_{FN}(f_{osc})}{SA_{FP}(f_{osc})} \tag{24}$$

The response spectra are calculated from accelerograms after Weber (2002) with a damping of $\zeta = 0.05$.

The amplitudes of waves parallel to rupture propagation differ from waves normal to propagation on top of the directivity effect. This variation depends on the azimuth and is larger only at high periods. The fault-normal response amplitude is larger than the fault-parallel response if directed (anti)parallel to the rupture. We model the ratio similar to Somerville et al. (1997)

$$\ln(FN/FP) = (b_1 + b_2 f_{osc}^{b_3}\cos(2(\theta - \theta_R))H(b_1 + b_2 f_{osc}^{b_3}) \tag{25}$$

where parameters b_i describe the relationship of the oscillatory frequency to the ratio, θ is the azimuth (Eq. (20)), and θ_R is the azimuth of the maximal ratio. The ratio azimuth is subject to assumptions as is its counterpart θ_E. The Heaviside function $H(\cdot)$ avoids negative values in the model, which would be equivalent to an undesired phase shift in the cosine term.

We introduced a functional form for oscillatory frequency dependence with four parameters in Eq. (25). We did not introduce a distance term and apply the model only to data with $r_{rup} \leq 50$ km.

6 Results

6.1 Topographic analysis

Landslides occurred mostly in tephra layers (Fig. 2a,b) covered by forests (Fig. 2d,e) and predominantly along the NE rupture segment. Nearly all landslides concentrated on hillslopes between 15° and 45° steep and a MAF ≈ 1 (Fig. 4a,c). Hillslope inclination and MAF were higher towards the landslide crown (Fig. 4b,d), indicating a progressive landslide failure starting from the crown, consistent with numerical simulations by Dang et al. (2016). TWI is linked to land cover and is highest in areas with rice paddies (Fig. 2i). Terrain with landslides has uniformly low TWI, thus we cannot evaluate the hydrological impact on the earthquake related landslides (e.g. Tang et al., 2018).

Most landslides originated at locations with amplified ground accelerations and steep hillslopes and ran out on flatter areas with less amplified ground acceleration. Landslides—interpreted as shear failure—start as mode II (in-plane shear) failure at the scarp and mode III (anti-plane shear) failure at the flanks (McClung, 1981; Fleming and Johnson, 1989; Martel, 2004). At later stages of the landslide rupture, mode I (widening) failure can also occur in the process (Martel, 2004). Simulations of elliptic landslides by Martel (2004) show that either the most compressive or the most tensile stresses are parallel to the major axis of the landslide, coinciding with the average landslide aspect. Yamada et al. (2013) and Yamada et al. (2018) show for

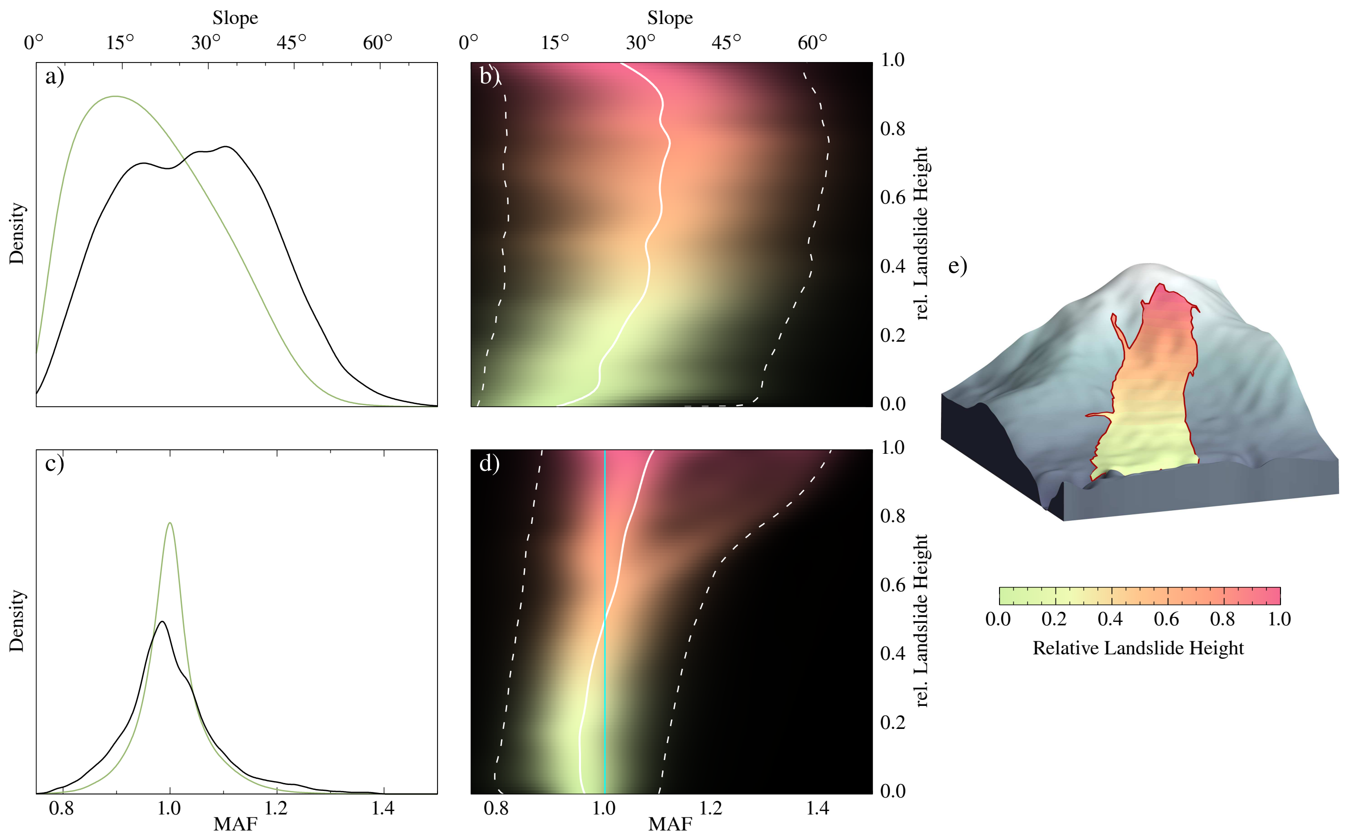

Figure 4. Distribution of hillslope inclination and MAF. The left column shows a) hillslope inclinations and c) MAF within the landslide affected area (green), and within the landslide areas (black). The right column presents b) hillslope inclinations and d) MAF in different segments of the landslide areas which is expressed as relative height. Segments towards to the toe (relative height 0.0–0.5) are in green and red towards the crown (relative height 0.5–1). The solid line is the mean, the dashed lines enclose the 95 % uncertainty range. The concept of relative height is illustrated for the Aso-Ohashi landslide in e). MAF<1 indicates attenuation and MAF>1 amplification of seismic waves due to topography. The cyan line in d) highlights MAF = 1, i.e. no amplification or attenuation.

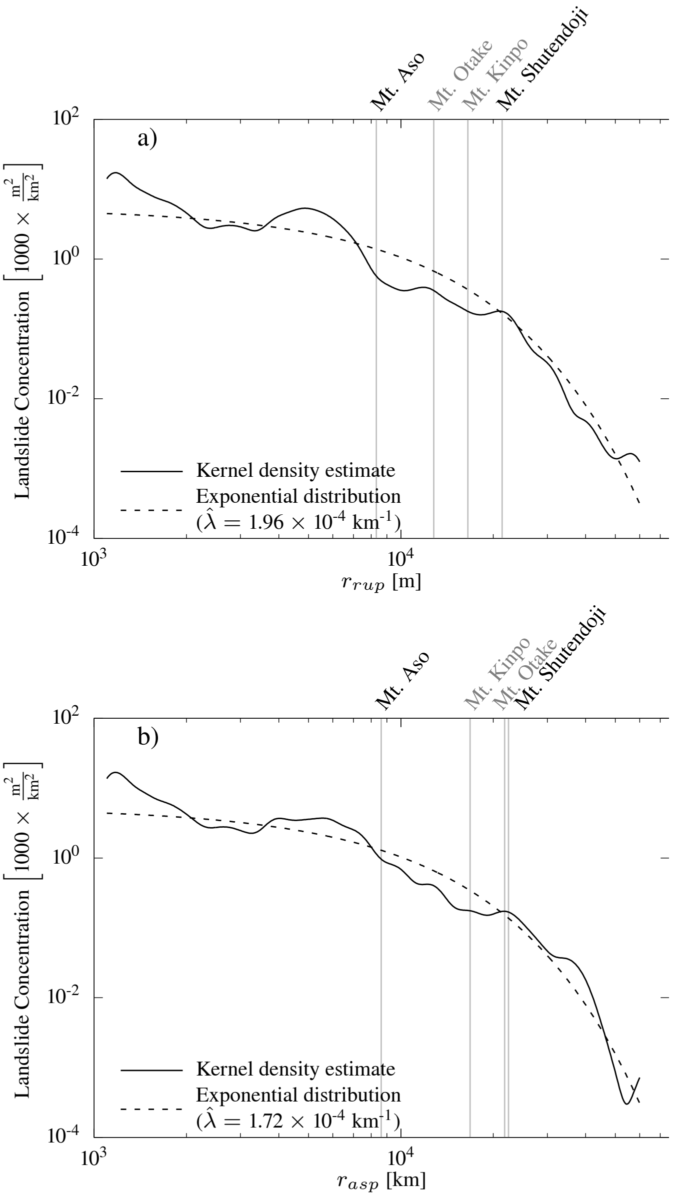

Figure 5. a) Landslide concentration with a) rupture distance r_{rup} and b) asperity distance $r_{asp}$of the Kumamoto earthquake landslides. The rate parameter of the the exponentially decaying landslide concentration is estimated by maximum likelihood. The distances to the four peaks shown in Fig. 1 are given. Densities change little with distance metric, as highlighted by the similiar kernel density estimates and the near-identical rate parameter estimates $\hat{\lambda}$. The landslide concentration for Mt. Aso depends more on the distance metric than for the other three locations. The more distant mountains have very similar concentrations despite differences in distances (in particular Mt. Otake). However, when compared to Fig. 7 Mt. Shutendoji has a higher landslide concentration than Mt. Kinpo and Mt. Otake, despite being the farthest away.

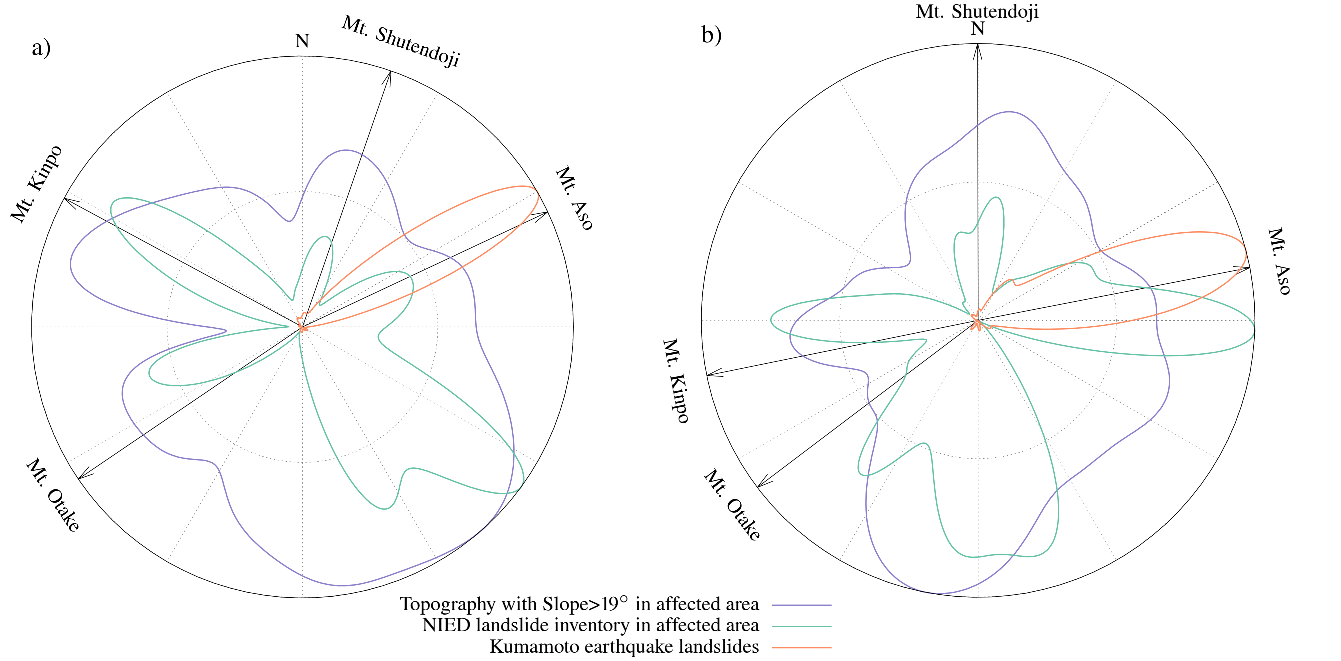

Figure 6. Density of hillslope inclinations with azimuth of the Kumamoto earthquake landslides with a) respect to the epicenter, and b) with respect to the asperity centroid. The densitites are normalized to their maxima.

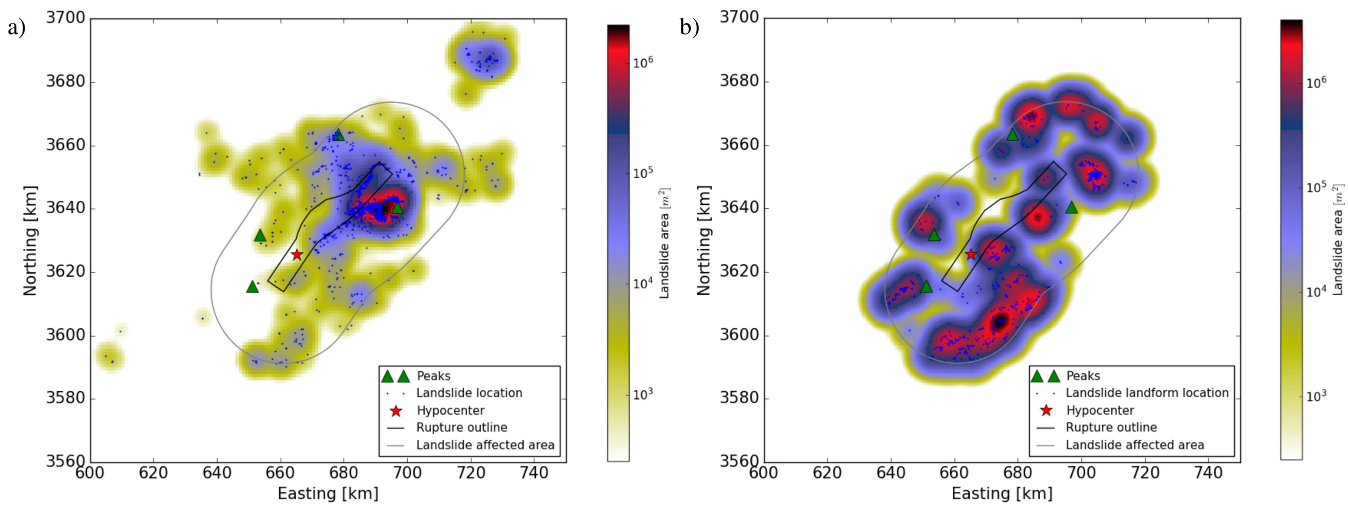

Figure 7. Spatial distribution of landslides. a) Coseismic landslides. The total landslide area at a location is shown as a color-coded smooth function in the background. b) Same as in (a) but for unspecified landslides within the landslide affected area of the Kumamoto earthquake.

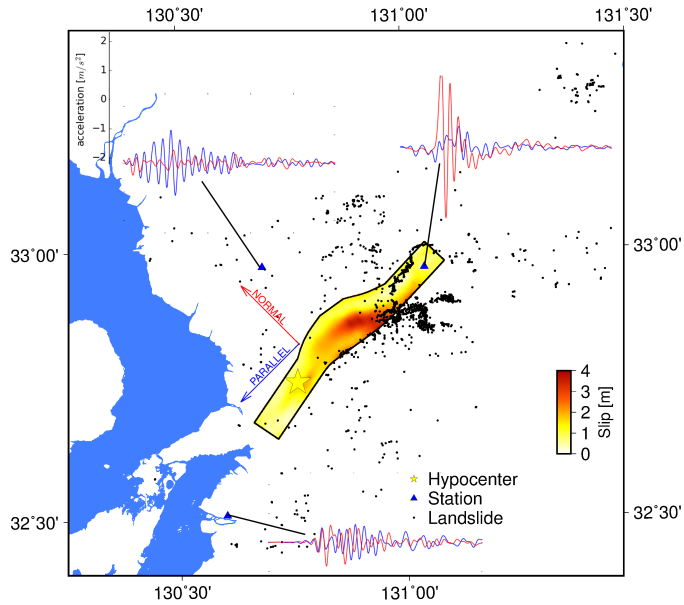

Figure 8. Characteristic waveforms observed in the vicinity of the rupture. The waveforms shown are low-passed filter at 1.2 Hz.

several japanese landslides that peak forces were aligned parallel to the long side of the landslides; Allstadt (2013) shows from waveform inversion for the Mt. Meager landslide that force and acceleration were parallel to the long side of the landslide source area.

Mt. Aso and its caldera and Mt. Shutendoji had a high density of landslides (Fig. 5), whereas Mt. Kinpo and Mt. Otake had none, despite being closer to the epicenter and at comparably close to the rupture (Fig. 5). All these locations have comparable rock type, land cover, comparable hillslope inclination, and MAF. Hence, lithology, land cover, and topographic characteristics are insufficient to explain the landslide distribution and concentration with respect to the hypocenter or the asperity.

The azimuthal density—with respect to the epicenter and asperity centroid—of the unspecified landslides follows to some extent the distribution of hillslope inclinations $> 19^\circ$ in the landslide affected area (Fig. 6). This similarity shows that the abundance of unspecified landslides mimics the steepness of topography in the region. Densities are higher towards Mt. Kinpo (NW), Mt. Otake (WSW), Mt. Shutendoji (N), Mt. Aso (NE), and the Kyushu Mts. (SE). The coseismic landslide distribution differs completely from the distributions of unspecified landslides and their surrounding topography, respectively, as nearly all landslides happened to the northeast of the epicenter close to the rupture plane (Fig. 7). Chen et al. (2017) identified only 29 landslide recactivations during the Kumamoto earthquake. The contrast between the distributions of unspecified landslides and earthquake related landslides indicates a contribution by the rupture process.

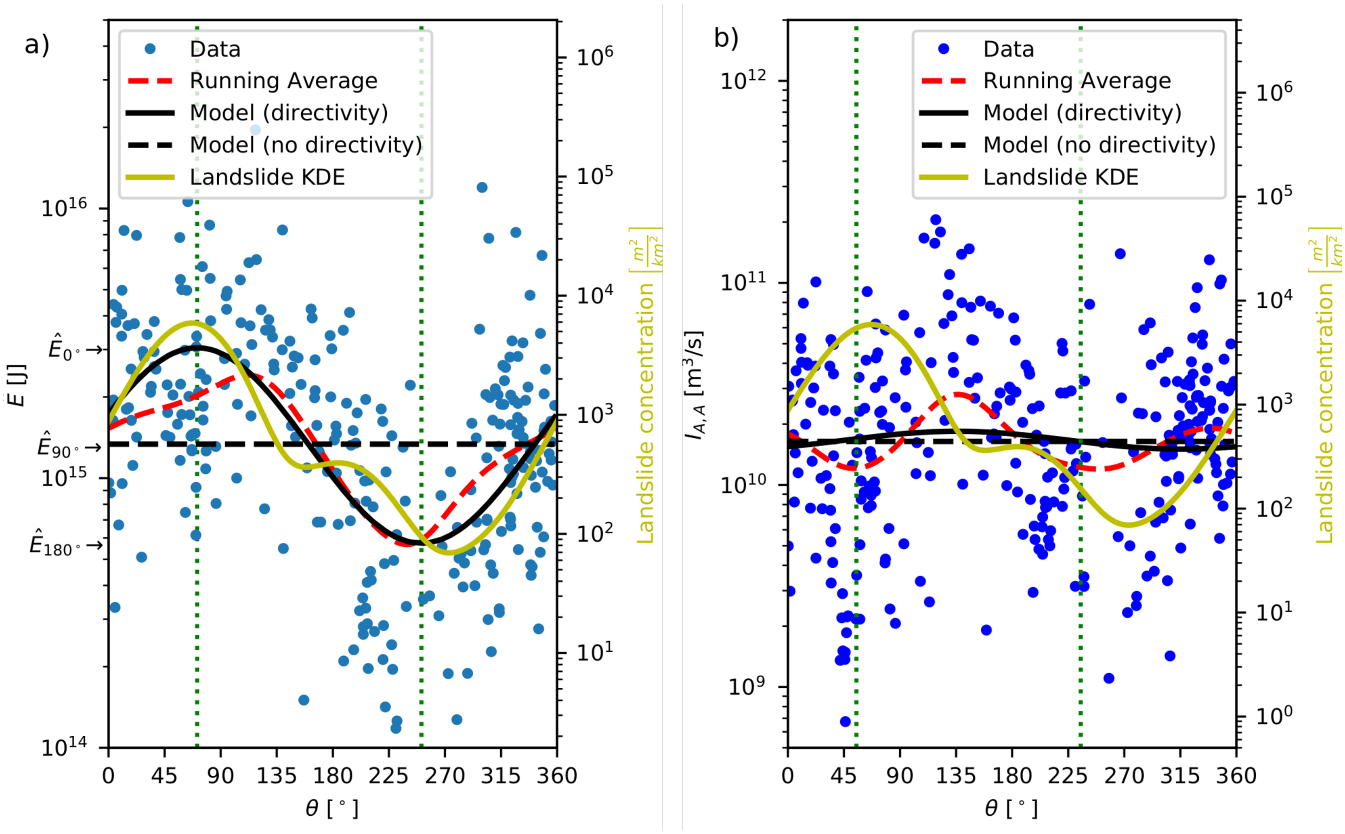

Figure 9. a) Energy estimates ($\hat{E}$) over azimuth. b) Same as in a) but for Arias intensity with correction for geometrical spreading ($I_{A,A}$).

6.2 Impact of finite source on ground motion and landslides

The results of the seismic analysis are given for waveforms, the basis for $\hat{E}$ and I_A, and response spectra, used for FN/FP. To the northeast, signals with forward-directivity are shorter in duration with one or few strong pulses (Fig. 8, top right). Waveforms with backward-directivity to the southwest of the rupture are longer with no dominant pulse (Fig. 8, bottom left). Waveforms parallel to the rupture have intermediate duration. Waveforms in either forward- or backward-direction have stronger amplitudes in the fault-normal direction, whereas waveforms outside the directivity-affected regions have stronger amplitudes in the fault-parallel direction (Fig. 8, top left).

We estimated energies $\hat{E}$ from the three-component waveforms. For the Arias intensity, both horizontal components are used. The geometrical spreading A is calculated according to Eq. (12) with a rupture length of L =53.5 km and width of W =24.0 km. Any remaining distance dependence has been corrected for by estimating and applying the attenuation parameter k (Eq. (13))

After the determination of k, $\hat{E}$ and $I_{A,A}$ are considered distance independent and can be investigated for azimuthal variations. With a reference point for the azimuth at the epicenter, $\hat{E}$ shows oscillating variations in amplitude with azimuth (Fig.

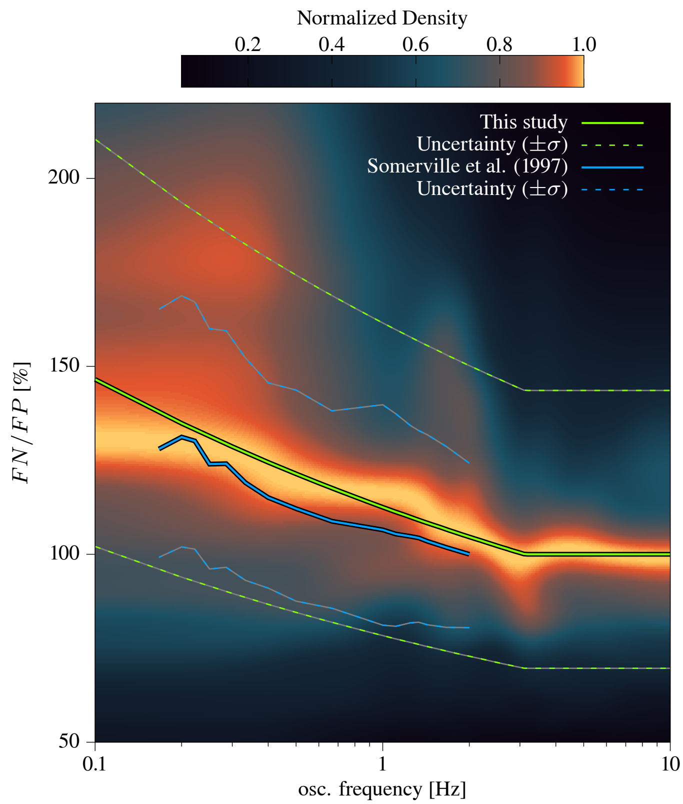

Figure 10. Kernel density estimate of the amplitude ratio of response spectra of fault-normal and fault-parallel components (FN/FP) with respect to oscillatory frequency. Beyond 2–3 Hz FN/FP variations cease as highlighted by our model and the model by Somerville et al. (1997).

9a), while $I_{A,A}$ exhibits a similar amplitude variations over the entire azimuthal range (Fig.9b). The running average based on a von Mises kernel ($\kappa_{vM} = 50$) of $\hat{E}$ and $I_{A,A}$ shows increased $\hat{E}$ between 45° and 135°, i.e. approximately parallel to the strike. Minimal values of $\hat{E}$ occur in the opposite direction (200°–300°). The running average of $I_{A,A}$ has several fluctuations but not as wide and large as that of $\hat{E}$. The azimuthal variation of $\hat{E}$ indicates the rupture directivity and the absence of large variations in $I_{A,A}$ indicates that the directivity effect is only evident at lower frequencies (compare with Fig. 3).

The azimuthal variation of $\hat{E}$ and $I_{A,A}$ is modelled according to Eq. (20). We estimate parameters for two scenarios:

- directivity is assumed, resulting in azimuthal variations, where a_E and a_I are free parameters,
- directivity is not assumed, resulting in no azimuthal variations with $a_E = a_I = 0$.

The two models are compared with the Bayesian Information Criterion (BIC, Schwarz, 1978) for a least squares fit:

$$BIC = n \ln N + N \ln \hat{\sigma}^2, \tag{26}$$

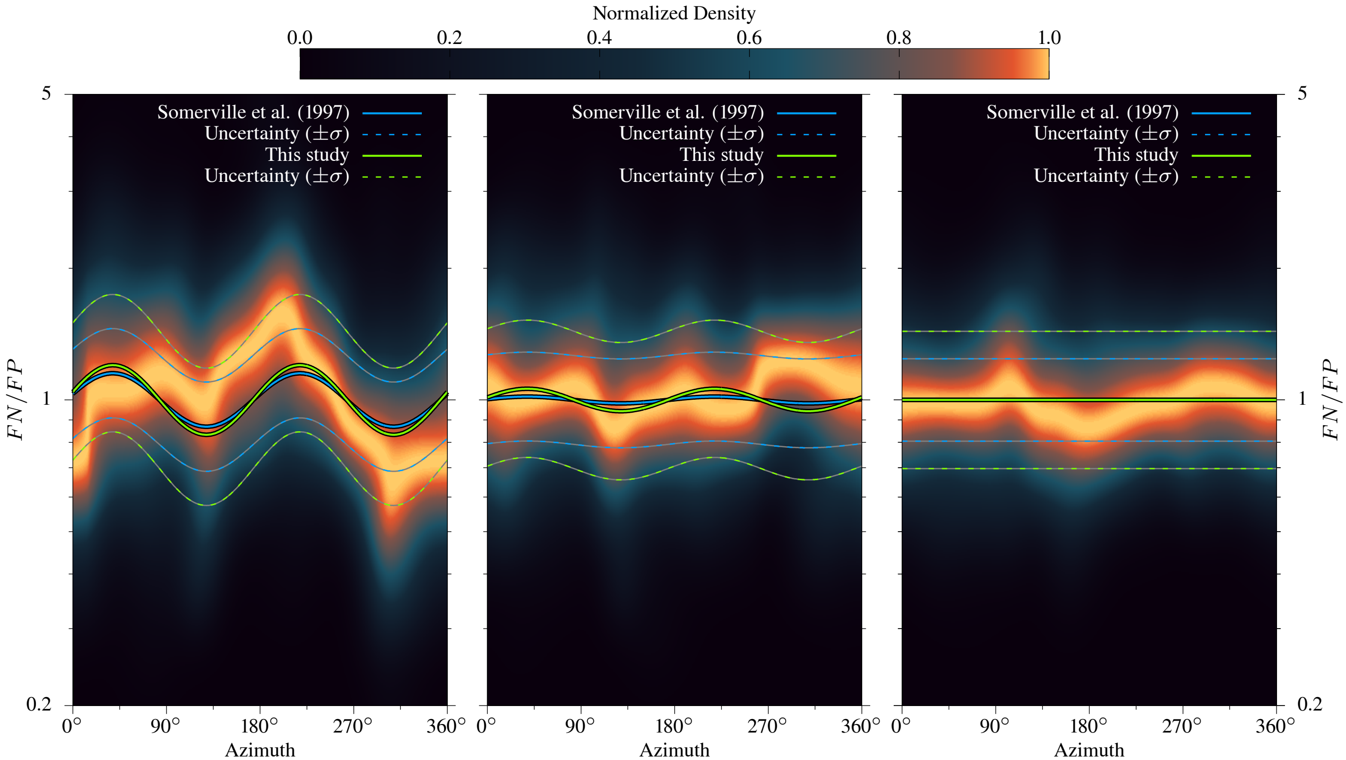

Figure 11. Kernel density estimate of FN/FP with azimuth obtained from response spectra for three different oscillatory frequency ranges: a) 0.1 – 1 Hz, b) 1.0 – 2.5 Hz, c) >2.5 Hz. For each plot, our FN/FP model and the model by Somerville et al. (1997) are shown for a) 0.55 Hz, b) 1.75 Hz, c) 4 Hz. As in Fig. 10, amplitudes decrease with increasing oscillatory frequency.

where n is the number of estimated parameters (n =4 for first case, n =2 for second case), N is the number of data, and $\hat{\sigma}^2$ is the variance of the model residuals. The model with the smaller BIC is preferable. The starting values of the parameters are the mean of $\hat{E}$ and $I_{A,A}$, no azimuthal variation (a_d =0), and the azimuths of the maximum of $\hat{E}_\theta$ and $I_{A,A,\theta}$ are set to the strike of the fault ($\theta_E = \theta_I = 225°$).

The directivity model for $\hat{E}$ follows the trend of the data and the running average closer than the model without directivity (Fig. 9a). According to BIC, the model with directivity is preferable ($BIC_{\text{directivity}}$ = -110, $BIC_{\text{no directivity}}$ = -11). In case of the Arias intensity, the difference in BIC between the two models is less compared to the azimuth-dependent energy (Fig. 9b). Here, the model without directivity is the preferred one ($BIC_{\text{directivity}}$ = 30, $BIC_{\text{no directivity}}$ = 22). In consequence, azimuthal variations in wave amplitudes and energy related to the directivity effect occur at lower frequencies.

The forward directivity waves contain a very strong low frequency pulse (Fig. 8). The pulse amplitude depends on the ratio of rupture and shear wave velocity and the length of the rupture (Spudich and Chiou, 2008). The forward directivity pulse is superimposed by high frequency signals in acceleration traces but becomes more prominent in velocity traces (Baker, 2007), due to its low frequency nature, i.e. below 1.6 Hz (Somerville et al., 1997).

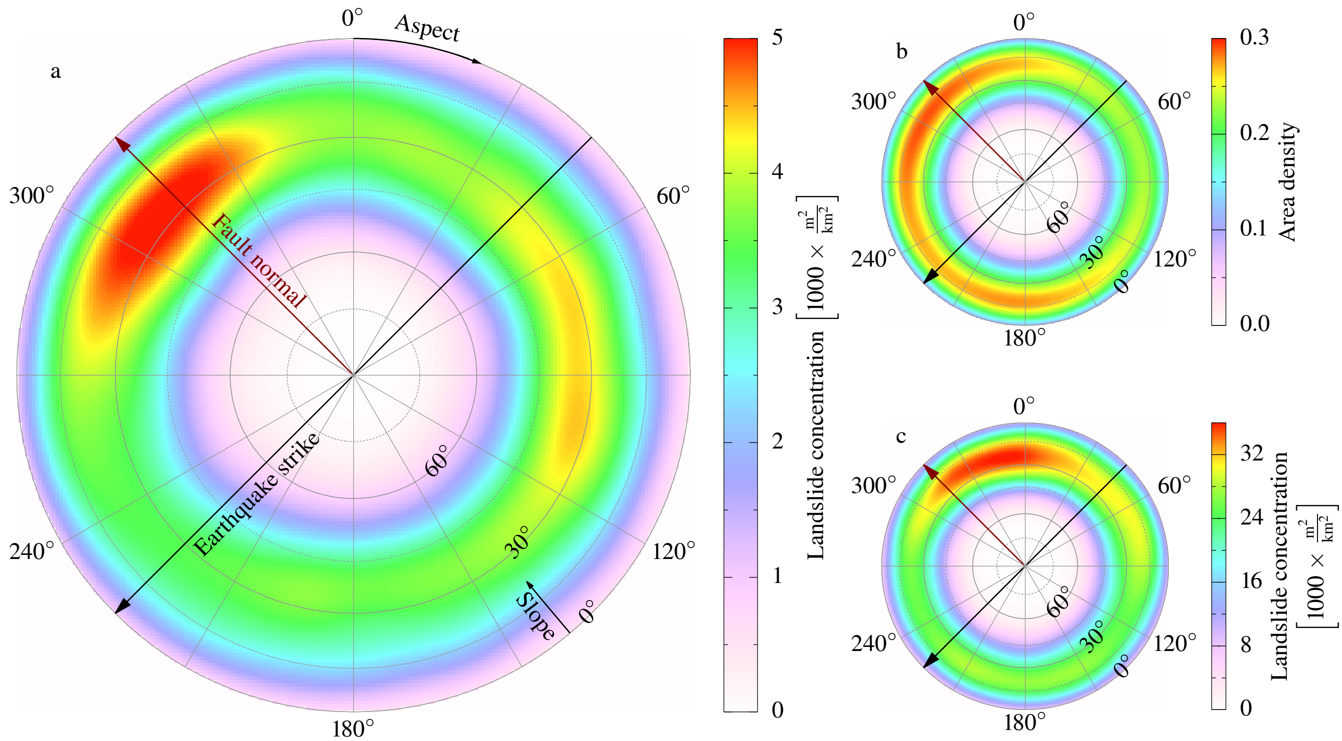

Figure 12. a) Aspect and hillslope inclination distribution within areas of the earthquake triggered landslides. This distribution is normalized by the distribution of the aspect of all hillslopes in the landslide affected area. The black line denotes the strike of the Kumamoto earthquake (225°) b) Distribution of aspect and hillslope inclination in the landslide affected area. c) Same as in a) but for unspecified landslides.

The low-frequency azimuthal variations are also reflected in the spectral response of the waveforms. Spectral accelerations of stations with r_{rup} ≤50 km were computed from 0.1 Hz to 5 Hz at intervals of 0.01 Hz for the fault-normal and fault-parallel component. The distribution of FN/FP shows decreasing azimuthal variability with increasing oscillatory frequency (Fig. 11, Fig. 11). FN/FP is most variable with azimuth at low oscillatory frequencies (0.1 – 1 Hz, Fig. 11a); variations are much smaller between 1 and 2.5 Hz (Fig. 11b); and nearly absent above 2.5 Hz (Fig. 11c). This decrease with frequency is captured by the FN/FP model (Eq. (25), Fig. 10). Since our model is an average over the covered distance, with an average rupture distance of 25.06 km, we compare it to the FN/FP model of Somerville et al. (1997) at 25 km (Fig. 10, Fig. 11). Both models show a similar decay with frequency with our model predicting a slightly higher FN/FP. Therefore, the wave polarity ratio related to rupture directivity is pronounced at lower frequencies and dissipates with increasing frequency, similar to the azimuthal variations observable in energy estimates (lower frequencies), but not in Arias intensity (higher frequencies).

The pattern of low-frequency ground motion is well reflected in that of the landslides. The azimuthal variation of $\hat{E}$ coincides with that of landslide concentration (Fig. 9). Both azimuth-dependent energy and landslide concentration have a similar trend with the maximum parallel to rupture direction and the minimum strike anti-parallel. The orientation of maximum FN/FP is also reflected in the landslide aspect. The northwest and east directions show higher landslide density (Fig. 12a). The highest

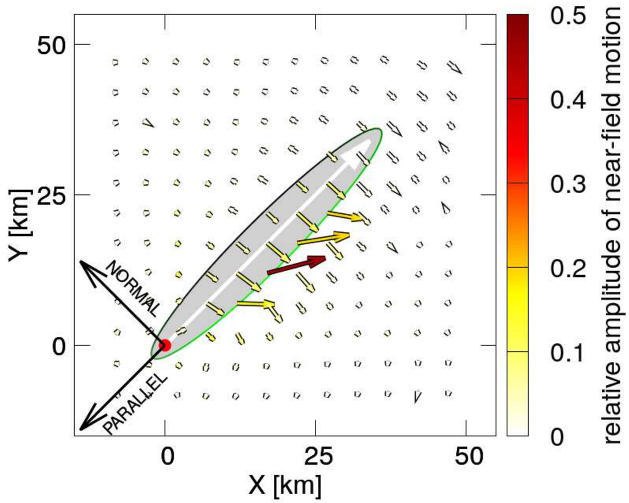

Figure 13. Orientation of horizontal peak-ground acceleration for the simulated waveforms. The arrow length scales with magnitude of acceleration. The simulated rupture plane is oriented as the rupture plane of the Kumamoto earthquake (strike: 225°, dip: 70°) and of elliptic shape (gray). The upper side is denoted by the green line, the lower half by black. The rupture process originated at the hypocenter (red dot) with circular propagation outwards (white arrow).

density of landslides has a northwestern aspect in agreement with maximum FN/FP, both perpendicular to the strike. The eastward increased density is mostly due to landslides very close to the rupture. A look at different distances reveals that the increased density of landslides facing east by southeast is at very short distances ($r_{rup} \leq 2.5$ km, Fig. 14), while the northwest facing landslides are further away (2.5 km $< r_{rup} \leq 6$ km). Only minor landslides are farther away with no specific pattern.

The distribution of aspect and hillslope inclination in the landslide affected area varies little with aspect (Fig. 12b).. The distinct northwest and east orientation of landslides is not an artefact of the orientation of the topography in the landslide affected area (12a,b). The unspecified landslides in the affected area have a near northward aspect and deviate by $\approx 30°$ from the earthquake triggered landslides (Fig. 12c). This highlights that the earthquake affects landslide locations (Fig. 6, 7); and will force failure on specific slopes facing in the direction of ground motion (Fig. 12, 14).

6.3 Ground motion model for Kumamoto

We derived two ground-motion models for Arias intensity from data with $r_{rup} \leq 150$ km (Tab. 1, Fig. 15). One model incorporates the azimuth-dependent seismic energy (Eq. (19)). The other is a conventional isotropic moment magnitude dependent model (Eq. (18)). The decay of Arias intensity with distance for both models fits well the running average and is proportional to the decrease in landslide density with distance. Variation of estimated energy is well covered by the model and spans more than two orders of magnitude resulting in a variation of Arias intensity of nearly one order of magnitude.

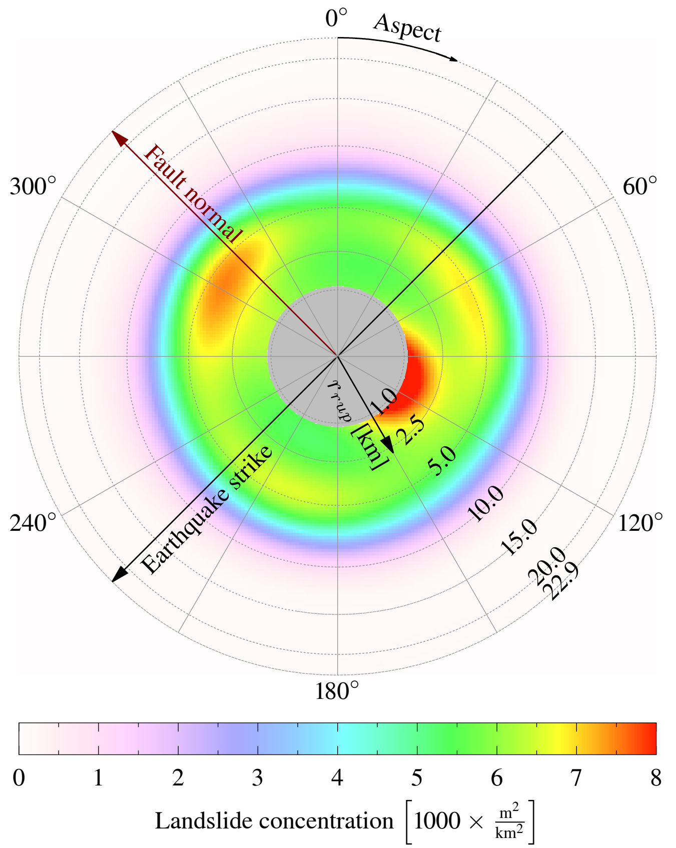

Figure 14. Distribution of landslides with aspect and rupture distance. The rupture distance is measured from the model by Kubo et al. (2016). This model does not completely reach the surface, truncanting distances below 1 km. The distribution has been normalized by the distribution of aspect of the affected area.

	model using $\hat{E}$	model using M_W
c_1	4.083	5.879
c_2	1.162×10^{-1}	-3.201×10^{-2}
c_3	-3.052×10^{-5}	-3.172×10^{-5}
c_4	-4.343×10^{-1}	-2.349×10^{0}
c_5		5.565×10^{-2}

Table 1. Parameters for ground-motion models

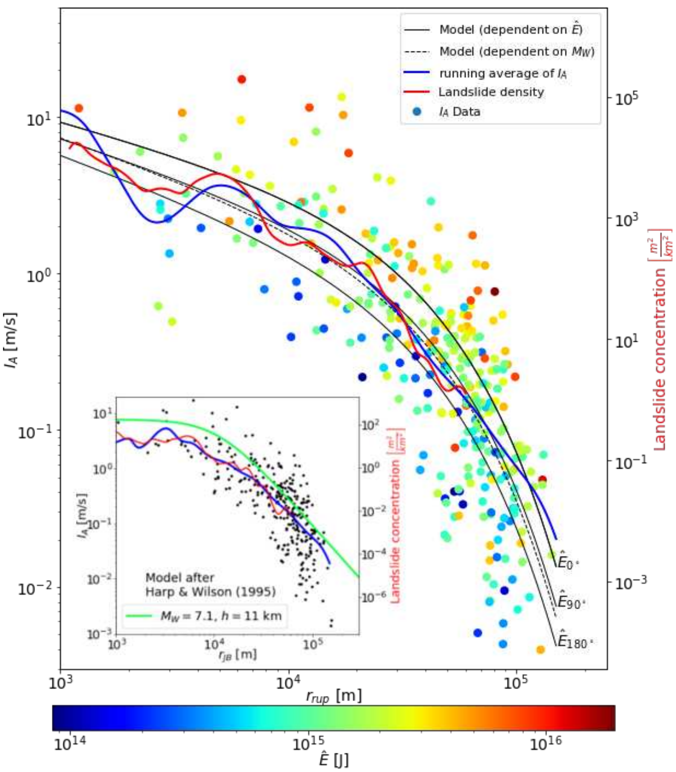

Figure 15. Ground motion model for I_A. The solid lines are the model with energy estimates for three different energy levels as in Fig. 9a. The inset figure shows for comparison the ground motion model of Harp and Wilson (1995) (green), landslide concentration density (red).

The magnitude based model is nearly equivalent to the energy based model with $\hat{E} = 1.2 \times 10^{15}$ J. This value is close to the average energy estimate found from energy estimates of the directivity model from Eq. (20) ($\hat{E} = 1.3 \times 10^{15}$ J). The closeness of the two values implies that the magnitude based model can be seen as an average over the azimuth of the energy based model.

7 Discussion

We provide a framework for characterizing coseismic landslides with an integrated approach of geomorphology and seismology emphasizing here the role of low-frequency seismic directivity and finite source. Given the observations of ground motion of the Kumamoto earthquake, two questions arise: (1) How specific is the observed ground motion, i.e. is the Kumamoto rupture particularly distinct? (2) As a rupture very close to the surface, how much does seismic near-field motion contribute? The second question arises, because many landslides occurred very close to the rupture plane. However, it is not possible to separate the observed waveforms into near-, intermediate-, and far-field terms. To investigate both questions, we computed theoretical waveforms after Haskell (1964); Savage (1966); Aki and Richards (2002) from a circular rupture on an elliptic finite source with constant rupture velocity in a homogeneous, isotropic, and unbound medium (see Appendix).

Despite the simplified assumptions behind this waveform model, low-frequency ground motions capture the most prominent features of the observed waveforms. Simulated waveforms close to the rupture plane change in polarity orientation towards east-west, while a strong fault-normal polarity appears at larger distances. A decomposition into a near-field term and combined intermediate- and far-field term reveals that the former highly contributes to the ground-motion at close distances. The impact of the near-field term may explain the dominance of east-facing landslides close to the rupture (Fig. 14).

The simulations also demonstrate the effect of directivity on estimates of radiated energy and Arias intensity. The azimuthal variations of simulated $\hat{E}$ are similar to the observed variations. The Arias intensity of the simulations also has azimuthal variations with the same characteristics as the energy estimate. These variations in Arias intensity are absent in the observed data, indicating that Arias intensity is more influenced by local heterogeneities and scattering than the energy estimates as these are ignored in the simulations.

The results show that the Arias intensity is not as susceptible to the directivity effect and variations in fault-normal to fault-parallel amplitudes as is the radiated energy: because of its higher sensitivity towards higher frequencies, these effects are masked by high-frequency effects such as wave scattering and a heterogeneous medium. We found that the radiation pattern related to the directivity effect is recoverable from energy estimates but not from Arias intensity. This low-frequency dependence is also seen in the response spectra ratios for FN/FP where directivity related amplitude variations with azimuth have been identified only for frequencies <2 Hz, and in agreement with previous work (Spudich et al., 2004; Somerville et al., 1997). We introduced a modified model for Arias intensity using site-dependent seismic energy estimates instead of the source-dependent seismic magnitude to better capture the effects of low-frequency ground motion.

The conventional magnitude-based, isotropic model and the azimuth-dependent seismic energy model correlate with the landslide concentration over distance (Fig. 15). As in Meunier et al. (2007) it is therefore feasible to use the ground-motion model to model the landslide concentration, $P_{ls}(I_A)$, by a linear relationship

$$\ln P_{ls}(I_A) = a_I + b_I \ln I_A \quad (27)$$

Azimuthal variations of landslide density correspond to azimuthal variations in seismic energy and can be described by a similar relationship

$$\ln P_{ls}(E) = a_E + b_E \cos(\theta - \theta_E) \quad (28)$$

For the Kumamoto earthquake data we estimate $a_I = 2.1$, $b_I = 2.6$ and $a_E = -31.5$, $b_E = 2.3$. The azimuth-dependent landslide concentration implies similar landslide concentrations at different distances from the rupture, thus partly explaining some of the deviation in Fig. 5 and Fig. 15.

Compared to the model of Harp and Wilson (1995) (Fig. 15) our model uses rupture-plane distance, as opposed to the Joyner-Boore distance (r_{JB}). When using the hypocentral depth as pseudodepth, the model of Harp and Wilson (1995) overpredicts I_A both at shorter and longer distances—irrespective of the pseudodepth at larger distances. This misestimate is most likely due to the lack of an additional distant dependent attenuation term in their model (Eq. (17)).

The use of MAF instead of curvature alone provides a proxy by how much a seismic wave is amplified (or attenuated) for a given wavelength and location. We show that both hillslope inclination and MAF tend to be lower towards the landslide toe (Fig. 4). This effect is linked to the convention that landslide polygons cover both the zone of depletion and accumulation. (Sato et al., 2017) consider the tephra layers rich in halloysite to be the main sliding surfaces indicating shallow landslides (Song et al., 2017). When relating coseismic landsliding to the seismic rupture, only the failure plane of the landslide matters, because this is the hillslope portion that failed under seismic acceleration. Chen et al. (2017) noted, for example, that landslide susceptibility and safety factor calculation depends on whether the entire landslide or only parts—scarp area or area of dislocated mass—are considered. The reconstruction of the landslide failure planes is limited to statistical assessments of landslide inventories (Domej et al., 2017; Marc et al., 2019). However, failure may have likely originated close to the crown and then progressively propagated downward the hillslope, because MAF > 1 indicates an amplification of ground motion towards the crown of the landslides.

Coseismic landslide locations have a uniformly low topographic wetness index, indicating that hydrology may have added little variability to the pattern of the earthquake triggered landslides; at least we could not trace any clear impact of soil moisture on the coseismic landslide pattern (Tang et al., 2018).

8 Conclusions

We investigated seismic waveforms and resulting landslide distribution of the 2016 Kumamoto earthquake, Japan. We demonstrate that ground motion at higher frequencies controls the isotropic (azimuth-independent) distance dependence of Arias intensity with landslide concentration. In addition, ground motion at lower frequencies influences landslide location and hillslope failure orientation, due to directivity and increased amplitudes normal to the fault, respectively. Topographic controls (hillslope inclination and MAF) are limited predictors of coseismic landslide occurrence, because areas with similar topographic and geological properties at similar distances from the rupture had widely differing landslide activity (Havenith et al., 2016; Massey et al., 2018). Nonetheless landslides concentrated only to the northeast of the earthquake rupture, while unspecified landslides have been identified throughout the affected region.

We introduced a modified model for Arias intensity using site-dependent radiated seismic energy estimates instead of the source-dependent seismic magnitude to better model low-frequency ground-motion in addition to the ground-motion at higher frequencies covered by the Arias intensity.

Compared to previous models widely used in landslide related ground motion characterization our model is based on state-of-the-art ground-motion models used in engineering seismology, which have two different distance terms, one for geometrical spreading and one for along-path attenuation. The latter is rare in landslide studies (e.g. Meunier et al., 2007; Massey et al., 2018). Our results emphasize that the attenuation term should be considered in ground-motion models, as the landslide concentration with distance mirrors such ground-motion models.

The effect of the earthquake rupture on the rupture process of the landslides results in landslide movements parallel to strongest ground-motion. Due to the surface proximity of the earthquake rupture plane, near-field ground motion influences

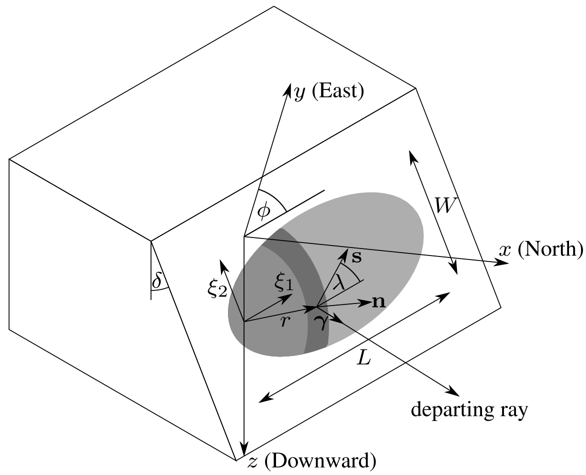

Figure A1. Setup of the rupture model. Gray ellipse represents the rupture: light gray area is unruptured, medium gray area is slipping, and the dark gray area is after slip arrest.

the aspect of close landslides to be east-southeast. The intermediate- and far-field motion of the earthquake promoted more landslides on northwest exposed hillslopes, an effect that overrides those of steepness and orientation of hillslopes in the region.

We highlight that coseismic landslide hazard estimation requires an integrated approach of both detailed ground-motion and topographic characterization. While the latter is well established for landslide hazard, ground-motion characterization has been only incorporated by simple means, i.e. without any azimuth-dependent finite rupture effects. Our results for the Kumamoto earthquake demonstrate that seismic waveforms can be reproduced by established methods from seismology. We suggest that these methods can improve landslide hazard assessment by including models for finite rupture effects.

Appendix A: Synthetic waveforms from displacement of a finite rupture

We illustrate the generation of ground displacement as a discontinuity across a rupture fault (e.g. Haskell, 1964, 1969; Anderson and Richards, 1975; Aki and Richards, 2002). The displacement for any point x at time t is given by

$$u_i(\mathbf{x},t) = \iint\limits_{\Sigma} c_{jkpq} \frac{\partial G_{ip}(D_j(\boldsymbol{\xi},t))}{\partial x_q} n_k d\Sigma \tag{A1}$$

where c is the fourth order elasticity tensor from Hooke's law, G is the Green's function describing the response of the medium, $\mathbf{D}(\boldsymbol{\xi},t)$ is the displacement on the fault with area Σ and coordinates $\boldsymbol{\xi}$, $\mathbf{n}$ is the fault normal vector. Summation over i,j,p,q is implied. While the surface integral is carried out numerically, the derivatives of the Green's function for an isotropic, homogeneous, and unbound medium can be solved analytically.

$$\frac{\partial}{\partial x_q} G_{ip}(D_j(\boldsymbol{\xi},t)) = \tag{A2a}$$

$$\frac{15\gamma_i\gamma_p\gamma_q - 3(\delta_{ip}\gamma_q + \delta_{iq}\gamma_p + \delta_{pq}\gamma_i)}{4\pi\rho r^4} \int_{\frac{r}{\alpha}}^{\frac{r}{\beta}} D_j(\boldsymbol{\xi}, t-\tau)\tau d\tau \tag{A2b}$$

$$+\frac{6\gamma_i\gamma_p\gamma_q - (\delta_{ip}\gamma_q + \delta_{iq}\gamma_p + \delta_{pq}\gamma_i)}{4\pi\rho\alpha^2 r^2} D_j\left(\boldsymbol{\xi}, t-\frac{r}{\alpha}\right) \tag{A2c}$$

$$-\frac{6\gamma_i\gamma_p\gamma_q - (2\delta_{ip}\gamma_q + \delta_{iq}\gamma_p + \delta_{pq}\gamma_i)}{4\pi\rho\beta^2 r^2} D_j\left(\boldsymbol{\xi}, t-\frac{r}{\beta}\right) \tag{A2d}$$

$$+\frac{\gamma_i\gamma_p\gamma_q}{4\pi\rho\alpha^3 r} \dot{D}_j\left(\boldsymbol{\xi}, t-\frac{r}{\alpha}\right) \tag{A2e}$$

$$-\frac{\gamma_i\gamma_p\gamma_q - \delta_{ip}\gamma_q}{4\pi\rho\beta^3 r} \dot{D}_j\left(\boldsymbol{\xi}, t-\frac{r}{\beta}\right) \tag{A2f}$$

where

$$r = |\mathbf{x} - \boldsymbol{\xi}| \text{ and } \gamma_i = \frac{x_i - \xi_i}{r} \tag{A3}$$

and δ_{ij} is Kronecker's delta. The terms in Eq. (A2) are commonly separated in groups with respect to their distance r. In Eq. (A2a) is the near-field (NF) term, as its amplitude decays with r^{-4}, it affects the immediate vicinty of a rupture only. Terms with a distance attenuation proportional to r^{-2} are called intermediate-field (IF) terms for P-waves (Eq. (A2c)) and S-waves (Eq. (A2d)). The remaining two terms are the far-field (FF) terms for P-waves (Eq. (A2e)) and S-waves (Eq. (A2f)) with a decay proportional to r^{-1}. A major difference between the NF and IF terms, and the FF terms is that the former depend on the slip on the rupture and they are the cause for static and dynamic displacement; whereas the latter are functions of the time derivative of slip and result in dynamic displacement only.

The slip function in time is related to the Yoffe function Yoffe (1951); Tinti et al. (2005) with rise time T. We use the slip distribution of Savage (1966) to describe the amplitude distribution of the slip on the rupture, as well as the elliptical fault shape and rupture propagation from Savage (1966). The slip amplitude is given by

$$D(\boldsymbol{\xi}) = D_0 \sqrt{1 - \left(\frac{\xi_1 - p\epsilon\frac{L}{2}}{\frac{L}{2}}\right)^2 - \left(\frac{\xi_2}{\frac{W}{2}}\right)^2} \tag{A4}$$

where D_0 is the maximum displacement at the center of the fault, L and W are the length and width of the fault, and p determines whether the rupture starts at the focus at the front of the rupture plane (strike-parallel, $p = 1$) or at the focus at the end (strike-anti-parallel, $p = -1$). The rupture originates in one of the two foci and propagates radially away from the source with constant velocity ζ and terminates when it reaches the rupture boundary. The slip vector $\hat{\mathbf{s}}$ describes the orientation of the displacement $D(\boldsymbol{\xi})$ on the fault plane. We follow the definition of $\hat{\mathbf{n}}$ and $\hat{\mathbf{s}}$ in terms of fault strike ϕ_s, dip δ, and rake λ from

Aki and Richards (2002):

$$\hat{\mathbf{n}} = \begin{pmatrix} -\sin\delta\sin\phi_s \\ \sin\delta\cos\phi_s \\ -\cos\delta \end{pmatrix} \tag{A5}$$

$$\hat{\mathbf{s}} = \begin{pmatrix} \cos\lambda\cos\phi_s + \cos\delta\sin\lambda\sin\phi_s \\ \cos\lambda\sin\phi_s - \cos\delta\sin\lambda\cos\phi_s \\ -\sin\lambda\sin\delta \end{pmatrix} \tag{A6}$$

The displacement vector $\mathbf{D}$ in Eq. (A2) is given by

$$\mathbf{D} = D(\boldsymbol{\xi})\hat{\mathbf{s}} \tag{A7}$$

We consider an isotropic medium and the elasticity tensor c from Eq. (A1) is

$$c_{jkpq} = \delta_{jk}\delta_{pq}\lambda + (\delta_{jp}\delta_{kq} + \delta_{jq}\delta_{kp})\mu \tag{A8}$$

where λ and μ are the Lamé parameters

$$\lambda = \rho(v_P^2 + 2\mu) \qquad \mu = \rho v_S^2 \tag{A9}$$

We set $\lambda = \mu$, resulting in the widely observed relation $v_P = v_S\sqrt{3}$.

With the assumptions outlined above it is possible to calculate the displacement of an earthquake at location x with 12 parameters (Fig. A1):

- fault size and orientation: length L, width W, strike ϕ, dip δ
- material: 1st and 2nd Lamé parameters λ and μ, density ρ (alternatively: compressional and shear wave velocities v_P and v_S and density ρ)
- rupture and slip: rupture velocity ζ, slip D_0, rise time T, rake λ, rupture orientation with respect to strike, p

The fault size and displacement of earthquakes are correlated with each other and are scaled to the magnitude. The number of parameters reduces to ten (nine if the Lamé constants are equal), when scaling relations (e.g. Leonard, 2010; Strasser et al., 2010) are used in combination with the seismic moment M_0. The moment can be decomposed in

$$M_0 = \mu A\bar{D} \tag{A10}$$

with shear modulus (2nd Lamé constant) μ, the rupture area—here an ellipse—$A = \frac{\pi}{4}LW$, and average displacement, $\bar{D}$ which follows from Eq. (A4) as $\bar{D} = \frac{2}{3}D_0$.

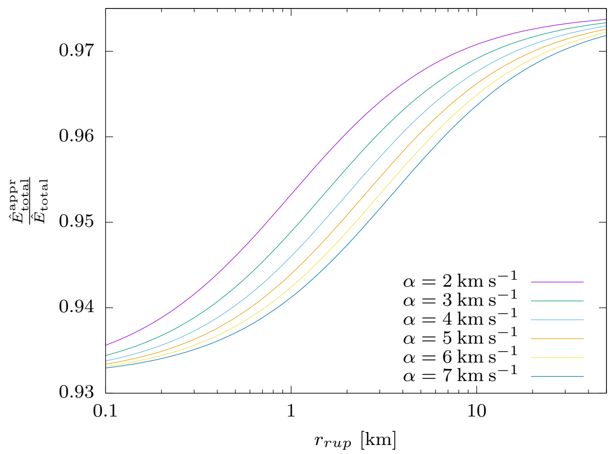

Figure B1. Ratio between the approximate and exact energy estimates for different P-wave velocities in the medium. The exact estimate assumes that P- and S-waves arrive at different velocities at the recording site, while the approximate estimate assumes that all waves arrive with shear wave velocity at the site. This approximation introduces only a minor underestimation, since most radiated energy is released as S-waves. The distance variation arises from the different distance and velocity dependencies of the intermediate-field terms and the far-field terms.

The results are not strictly comparable to observed data due to the models simplicity. The computed amplitudes will be smaller than observed values, because no free surface is assumed. Assuming a free surface would nearly double the amplitudes from wave reflection, as well as the amplifications from wave transmissions (from high to low velocity zones). Only direct waves are computed, and effects of reflections of different layers are not covered due to the isotropy and homogeneity. Corresponding waveforms—in particular surface waves—are not exhibited. However, the purpose of this model is to show (1) the general behavior of waveforms in the vicinity of a rupture, which is dominated by direct waves, and (2) how amplitudes distribute relatively in space.

Appendix B: Radiated seismic energy estimation

The exact calculation of radiated seismic energy is challenging. One simplifying assumption is that all waves arrive at the site with shear wave speed, which is a very good approximation for the far-field term. The reasoning can be justified from a theoretical perspective: For most earth media the ratio between the P-wave velocity α and S-wave velocity β is

$$\frac{\alpha}{\beta} = \sqrt{3} \tag{B1}$$

From this and Eq. A2e and A2f follows that the amplitude of compressional waves is $\approx \frac{1}{\sqrt{3}^3}$ of the shear wave amplitude. If we say that the P-wave train has a similar duration as the S-wave train, than the energy contribution of the P-waves with respect to the S-waves becomes $(\frac{1}{\sqrt{3}^3})^2 = \frac{1}{27}$. The total energy of a signal is (Rudnicki and Freund, 1981)

$$E_{total} = E_P + E_S \tag{B2}$$

and can be estimated by

$$\hat{E}_{total} = \alpha_S a IV2_\alpha + \beta_S a IV2_\beta, \tag{B3}$$

with the integrated squared velocity ($IV2$) for P- and S-waves from Eq. 7, the P- and S- wave velocities α_P and α_S at the recording site, and a constant a covering the remaining factors which are identical for both terms (compare with Eq. 8). If we express the energy contribution of P-waves in terms of S-waves, we can summarize the above relation to

$$\hat{E}_{total} = aIV2_\beta \left(\frac{\alpha_P}{27} + \beta_S\right) \tag{B4}$$

$$= aIV2_\beta \left(\frac{\beta_S\sqrt{3}}{27} + \beta_S\right) \tag{B5}$$

$$\approx aIV2_\beta \left(\frac{\beta_S}{27} + \beta_S\right). \tag{B6}$$

The last expression is differs only by 2.6 % from the exact term. While slightly underestimating the energy, this aproximate definition of using α_S instead of β_S does not require the identification of P- and S- waves. This is useful, since at short distances the S-wave train is usually inseparable from the P-wave train.

At shorter distances, the intermediate-field term needs also to be taken into consideration. The amplitude of the intermediate term decays with r^2 (Eq. A2c, A2d), while the far-field amplitude decays with r (Eq. A2e, A2f). That is, the amplitude scales by distance and velocities and thus the $IV2$ are

$$IV2_\alpha = \alpha^{-4} r^{-2}(r^{-1} + \alpha^{-1})^2, \tag{B7}$$

$$IV2_\beta = \beta^{-4} r^{-2}(r^{-1} + \beta^{-1})^2. \tag{B8}$$

Again replacing all P-wave terms by S-wave terms and the total energy becomes

$$\hat{E}_{total} = \alpha_S a IV2_\alpha + \beta_S a IV2_\beta \tag{B9}$$

$$= ar^{-2}\left(\alpha_S \alpha^{-4}(r^{-1} + \alpha^{-1})^2 + \beta_S \beta^{-4}(r^{-1} + \beta^{-1})^2\right) \tag{B10}$$

$$= ar^{-2}\left(\sqrt{3}^{-3}\beta_S \beta^{-4}(r^{-1} + \sqrt{3}^{-1}\beta^{-1})^2 + \beta_S \beta^{-4}(r^{-1} + \beta^{-1})^2\right) \tag{B11}$$

$$\tag{B12}$$

With the assumption that $\alpha_S = \beta_S$, Eq. B10 becomes

$$\hat{E}^{appr}_{total} \approx ar^{-2}\left(\beta_S \alpha^{-4}(r^{-1} + \alpha^{-1})^2 + \beta_S \beta^{-4}(r^{-1} + \beta^{-1})^2\right) \tag{B13}$$

$$= ar^{-2}\left(\sqrt{3}^{-4}\beta_S \beta^{-4}(r^{-1} + \sqrt{3}^{-1}\beta^{-1})^2 + \beta_S \beta^{-4}(r^{-1} + \beta^{-1})^2\right) \tag{B14}$$

The ratio between the approximation and the exact solution is

$$\frac{\hat{E}_{total}^{appr}}{\hat{E}_{total}} = \frac{\sqrt{3}^{-4}(r^{-1}+\sqrt{3}^{-1}\beta^{-1})^2+(r^{-1}+\beta^{-1})^2}{\sqrt{3}^{-3}(r^{-1}+\sqrt{3}^{-1}\beta^{-1})^2+(r^{-1}+\beta^{-1})^2} \tag{B15}$$

The two limits with respect to distance are

$$\lim_{r\to 0}\frac{\hat{E}_{total}^{appr}}{\hat{E}_{total}} = \frac{\sqrt{3}^{-4}+1}{\sqrt{3}^{-3}+1} \tag{B16}$$

$$\approx 0.932 \tag{B17}$$

$$\lim_{r\to \infty}\frac{\hat{E}_{total}^{appr}}{\hat{E}_{total}} = \frac{\sqrt{3}^{-5}+1}{\sqrt{3}^{-6}+1} \tag{B18}$$

$$\approx 0.974 \tag{B19}$$

The second limit is identical to the far-field case derived above. The two limits show that even in the range of the intermediate-field term, the energy estimate deviates little when assuming that all waves arrive with β_S at the recording site. A comparison of the approximate energy estimate and the exact estimate as a function of distance and velocity is shown in Fig. B1.

Acknowledgements. We highly appreciate the help of Tomotaka Iwata and Kimiyuki Asano for providing links to additional seismic data from the municipal and NIED networks and several helpful discussions on the specifics of the data. We are sincerely grateful to Takashi Oguchi, Yuichi Hayakawa, Hitoshi Saito and Yasutaka Haneda for the field trip to the Aso region and fruitful discussions. Thanks to Arno Zang and Odin Marc for various discussions and comments.

Sebastian von Specht, Ugur Ozturk, and Georg Veh acknowledge support from the DFG research training group "Natural Hazards and Risks in a Changing World" (Grant No. GRK 2043/1).

References

Aki, K. and Richards, P. G.: Quantitative seismology, 2002.

Allstadt, K.: Extracting source characteristics and dynamics of the August 2010 Mount Meager landslide from broadband seismograms, Journal of Geophysical Research: Earth Surface, 118, 1472–1490, https://doi.org/10.1002/jgrf.20110, http://doi.wiley.com/10.1002/jgrf.20110, 2013.

Allstadt, K. E., Jibson, R. W., Thompson, E. M., Massey, C. I., Wald, D. J., Godt, J. W., and Rengers, F. K.: Improving Near-Real-Time Coseismic Landslide Models: Lessons Learned from the 2016 Kaikoura, New Zealand, Earthquake, Bulletin of the Seismological Society of America, 108, 1649–1664, https://doi.org/10.1785/0120170297, https://pubs.geoscienceworld.org/ssa/bssa/article/108/3B/1649/529880/Improving-NearRealTime-Coseismic-Landslide-Models, 2018.

Anderson, J. G. and Richards, P. G.: Comparison of Strong Ground Motion from Several Dislocation Models*, Geophysical Journal of the Royal Astronomical Society, 42, 347–373, https://doi.org/10.1111/j.1365-246X.1975.tb05866.x, https://academic.oup.com/gji/article-lookup/doi/10.1111/j.1365-246X.1975.tb05866.x, 1975.

Arias, A.: MEASURE OF EARTHQUAKE INTENSITY., Tech. rep., Massachusetts Inst. of Tech., Cambridge. Univ. of Chile, Santiago de Chile, 1970.

Asano, K. and Iwata, T.: Source rupture processes of the foreshock and mainshock in the 2016 Kumamoto earthquake sequence estimated from the kinematic waveform inversion of strong motion data, Earth, Planets and Space, 68, 147, https://doi.org/10.1186/s40623-016-0519-9, http://earth-planets-space.springeropen.com/articles/10.1186/s40623-016-0519-9, 2016.

Baker, J. W.: Quantitative Classification of Near-Fault Ground Motions Using Wavelet Analysis, Bulletin of the Seismological Society of America, 97, 1486–1501, https://doi.org/10.1785/0120060255, https://pubs.geoscienceworld.org/bssa/article/97/5/1486-1501/146511, 2007.

Bernard, P. and Madariaga, R.: a New Asymptotic Method for the Modeling of Near-Field Accelerograms, Bulletin of the Seismological Society of America, 74, 539–557, 1984.

Böhner, J. and Selige, T.: Spatial prediction of soil attributes using terrain analysis and climate regionalisation, SAGA - Analysis and Modelling Applications, 115, 13–27, 2006.

Boore, D. M. and Bommer, J. J.: Processing of strong-motion accelerograms: Needs, options and consequences, Soil Dynamics and Earthquake Engineering, 25, 93–115, https://doi.org/10.1016/j.soildyn.2004.10.007, 2005.

Bora, S. S., Scherbaum, F., Kuehn, N., Stafford, P., and Edwards, B.: Development of a Response Spectral Ground-Motion Prediction Equation (GMPE) for Seismic-Hazard Analysis from Empirical Fourier Spectral and Duration Models, Bulletin of the Seismological Society of America, 105, 2192–2218, https://doi.org/10.1785/0120140297, https://pubs.geoscienceworld.org/bssa/article/106/3/1235-1253/332448https://pubs.geoscienceworld.org/bssa/article/105/4/2192-2218/332224, 2015.

Bray, J. D. and Rodriguez-Marek, A.: Characterization of forward-directivity ground motions in the near-fault region, Soil Dynamics and Earthquake Engineering, 24, 815–828, https://doi.org/10.1016/j.soildyn.2004.05.001, http://linkinghub.elsevier.com/retrieve/pii/S0267726104000703, 2004.

Bray, J. D. and Travasarou, T.: Simplified Procedure for Estimating Earthquake-Induced Deviatoric Slope Displacements, Journal of Geotechnical and Geoenvironmental Engineering, 133, 381–392, https://doi.org/10.1061/(ASCE)1090-0241(2007)133:4(381), 2007.

Brune, J. N.: Tectonic stress and the spectra of seismic shear waves from earthquakes, Journal of Geophysical Research, 75, 4997–5009, https://doi.org/10.1029/JB075i026p04997, http://doi.wiley.com/10.1029/JB075i026p04997, 1970.

Campillo, M. and Plantet, J.: Frequency dependence and spatial distribution of seismic attenuation in France: experimental results and possible interpretations, Physics of the Earth and Planetary Interiors, 67, 48–64, https://doi.org/10.1016/0031-9201(91)90059-Q, http://linkinghub.elsevier.com/retrieve/pii/003192019190059Q, 1991.

Chen, C.-W., Chen, H., Wei, L.-W., Lin, G.-W., Iida, T., and Yamada, R.: Evaluating the susceptibility of landslide landforms in Japan using slope stability analysis: a case study of the 2016 Kumamoto earthquake, Landslides, 14, 1793–1801, https://doi.org/10.1007/s10346-017-0872-1, http://link.springer.com/10.1007/s10346-017-0872-1, 2017.

Chigira, M. and Yagi, H.: Geological and geomorphological characteristics of landslides triggered by the 2004 Mid Niigta prefecture earthquake in Japan, Engineering Geology, 82, 202–221, https://doi.org/10.1016/j.enggeo.2005.10.006, 2006.

Choy, G. L. and Cormier, V. F.: Direct measurement of the mantle attenuation operator from broadband P and S Waveforms, Journal of Geophysical Research: Solid Earth, 91, 7326–7342, https://doi.org/10.1029/JB091iB07p07326, http://doi.wiley.com/10.1029/JB091iB07p07326, 1986.

Dadson, S. J., Hovius, N., Chen, H., Dade, W. B., Lin, J.-C., Hsu, M.-L., Lin, C.-W., Horng, M.-J., Chen, T.-C., Milliman, J., and Stark, C. P.: Earthquake-triggered increase in sediment delivery from an active mountain belt, Geology, 32, 733, https://doi.org/10.1130/G20639.1, https://pubs.geoscienceworld.org/geology/article/32/8/733-736/29559, 2004.

Dang, K., Sassa, K., Fukuoka, H., Sakai, N., Sato, Y., Takara, K., Quang, L. H., Loi, D. H., Van Tien, P., and Ha, N. D.: Mechanism of two rapid and long-runout landslides in the 16 April 2016 Kumamoto earthquake using a ring-shear apparatus and computer simulation (LS-RAPID), Landslides, 13, 1525–1534, https://doi.org/10.1007/s10346-016-0748-9, http://dx.doi.org/10.1007/s10346-016-0748-9http://link.springer.com/10.1007/s10346-016-0748-9, 2016.

Domej, G., Bourdeau, C., Lenti, L., Martino, S., and Pluta, K.: Mean landslide geometries inferred from globla database, 94 Italian Journal of Engineering Geology and Environment, 2, 87–107, https://doi.org/10.4408/IJEGE.2017-02.O-05, 2017.

Fan, X., Scaringi, G., Xu, Q., Zhan, W., Dai, L., Li, Y., Pei, X., Yang, Q., and Huang, R.: Coseismic landslides triggered by the 8th August 2017 Ms 7.0 Jiuzhaigou earthquake (Sichuan, China): factors controlling their spatial distribution and implications for the seismogenic blind fault identification, Landslides, 15, 967–983, https://doi.org/10.1007/s10346-018-0960-x, http://link.springer.com/10.1007/s10346-018-0960-x, 2018.

Festa, G., Zollo, A., and Lancieri, M.: Earthquake magnitude estimation from early radiated energy, Geophysical Research Letters, 35, L22 307, https://doi.org/10.1029/2008GL035576, http://doi.wiley.com/10.1029/2008GL035576, 2008.

Fleming, R. W. and Johnson, A. M.: Structures associated with strike-slip faults that bound landslide elements, Engineering Geology, 27, 39–114, https://doi.org/10.1016/0013-7952(89)90031-8, http://linkinghub.elsevier.com/retrieve/pii/0013795289900318, 1989.

Frankel, A.: Rupture Process of the M 7.9 Denali Fault, Alaska, Earthquake: Subevents, Directivity, and Scaling of High-Frequency Ground Motions, Bulletin of the Seismological Society of America, 94, S234–S255, https://doi.org/10.1785/0120040612, https://pubs.geoscienceworld.org/bssa/article/94/6B/S234-S255/146877, 2004.

Gorum, T., Fan, X., van Westen, C. J., Huang, R. Q., Xu, Q., Tang, C., and Wang, G.: Distribution pattern of earthquake-induced landslides triggered by the 12 May 2008 Wenchuan earthquake, Geomorphology, 133, 152–167, https://doi.org/10.1016/j.geomorph.2010.12.030, http://dx.doi.org/10.1016/j.geomorph.2010.12.030, 2011.

Gorum, T., Korup, O., van Westen, C. J., van der Meijde, M., Xu, C., and van der Meer, F. D.: Why so few? Landslides triggered by the 2002 Denali earthquake, Alaska, Quaternary Science Reviews, 95, 80–94, https://doi.org/10.1016/j.quascirev.2014.04.032, http://dx.doi.org/10.1016/j.quascirev.2014.04.032, 2014.

Hanks, T. C. and Kanamori, H.: A moment magnitude scale, Journal of Geophysical Research, 84, 2348, https://doi.org/10.1029/JB084iB05p02348, http://doi.wiley.com/10.1029/JB084iB05p02348, 1979.

Harp, E. L. and Wilson, R. C.: Shaking Intensity Thresholds for Rock Falls and Slides : Evidence from 1987 Whittier Narrows and Superstition Hills Earthquake Strong-Motion Records, Bulletin of the Seismological Society of America, 85, 1739–1757, 1995.

Haskell, N.: Determination of earthquake energy release and ML using TERRAscope, Bulletin of the Seismological Society of America, 59, 865–908, 1969.

Haskell, N. A.: Total energy and energy spectral density of elastic wave radiation from propagating faults, Bulletin of the Seismological Society of America, 54, 1811–1841, http://www.bssaonline.org/content/54/6A/1811.short, 1964.

Havenith, H. B., Torgoev, A., Schlögel, R., Braun, A., Torgoev, I., and Ischuk, A.: Tien Shan Geohazards Database: Landslide susceptibility analysis, Geomorphology, 249, 32–43, https://doi.org/10.1016/j.geomorph.2015.03.019, http://dx.doi.org/10.1016/j.geomorph.2015.03.019, 2015.

Havenith, H.-B., Torgoev, A., Braun, A., Schlögel, R., and Micu, M.: A new classification of earthquake-induced landslide event sizes based on seismotectonic, topographic, climatic and geologic factors, Geoenvironmental Disasters, 3, 6, https://doi.org/10.1186/s40677-016-0041-1, http://geoenvironmental-disasters.springeropen.com/articles/10.1186/s40677-016-0041-1, 2016.

Hovius, N. and Meunier, P.: Earthquake ground motion and patterns of seismically induced landsliding, in: Landslides, edited by Clague, J. J. and Stead, D., pp. 24–36, Cambridge University Press, Cambridge, https://doi.org/10.1017/CBO9780511740367.004, https://www.cambridge.org/core/product/identifier/9780511740367{%}23c00206-3-1/type/book{_}part, 2012.

Ji, C., Helmberger, D. V., Wald, D. J., and Ma, K.-F.: Slip history and dynamic implications of the 1999 Chi-Chi, Taiwan, earthquake, Journal of Geophysical Research: Solid Earth, 108, https://doi.org/10.1029/2002JB001764, http://doi.wiley.com/10.1029/2002JB001764, 2003.

Jibson, R. W.: Predicting Earthquake-Induced Landslide Displacements Using Newmark's Sliding Block Analysis, Transportation Research Record, 1411, 9–17, 1993.

Jibson, R. W.: Regression models for estimating coseismic landslide displacement, Engineering Geology, 91, 209–218, https://doi.org/10.1016/j.enggeo.2007.01.013, http://linkinghub.elsevier.com/retrieve/pii/S0013795207000300, 2007.

Jibson, R. W., Harp, E. L., and Michael, J. A.: A method for producing digital probabilistic seismic landslide hazard maps, Engineering Geology, 58, 271–289, https://doi.org/10.1016/S0013-7952(00)00039-9, 2000.

Kanamori, H., Mori, J. I. M., Hauksson, E., Heaton, T. H., Hutton, K., and Jones, L. M.: Determination of Earthquake Energy Release and, Bulletin of the Seismological Society of America, 83, 330–346, 1993.

Keefer, D. K.: Landslides caused by earthquakes, Geological Society of America Bulletin, 95, 406–421, 1984.

Koketsu, K., Miyake, H., and Suzuki, H.: Japan Integrated Velocity Structure Model Version 1, Proceedings of the 15th World Conference on Earthquake Engineering, pp. 1–4, http://www.iitk.ac.in/nicee/wcee/article/WCEE2012{_}1773.pdf, 2012.

Kramer, S. L.: Geotechnical earthquake engineering. In prentice–Hall international series in civil engineering and engineering mechanics, Prentice-Hall, New Jersey, 1996.

Kubo, H., Suzuki, W., Aoi, S., and Sekiguchi, H.: Source rupture processes of the 2016 Kumamoto, Japan, earthquakes estimated from strong-motion waveforms, Earth, Planets and Space, 2016, 1–13, https://doi.org/10.1186/s40623-016-0536-8, 2016.

Lee, C.-T.: Re-Evaluation of Factors Controlling Landslides Triggered by the 1999 Chi–Chi Earthquake, in: Earthquake-Induced Landslides, no. June in Springer Natural Hazards, pp. 213–224, Springer Berlin Heidelberg, Berlin, Heidelberg, https://doi.org/10.1007/978-3-642-32238-9_22, http://link.springer.com/10.1007/978-981-10-2935-6http://link.springer.com/10.1007/978-3-642-32238-9{_}22, 2013.

Leonard, M.: Earthquake Fault Scaling: Self-Consistent Relating of Rupture Length, Width, Average Displacement, and Moment Release, Bulletin of the Seismological Society of America, 100, 1971–1988, https://doi.org/10.1785/0120090189, https://pubs.geoscienceworld.org/bssa/article/100/5A/1971-1988/325106, 2010.

Marc, O., Hovius, N., Meunier, P., Gorum, T., and Uchida, T.: A seismologically consistent expression for the total area and volume of earthquake-triggered landsliding, Journal of Geophysical Research: Earth Surface, 121, 640–663, https://doi.org/10.1002/2015JF003732, http://doi.wiley.com/10.1002/2015JF003732, 2016.

Marc, O., Meunier, P., and Hovius, N.: Prediction of the area affected by earthquake-induced landsliding based on seismological parameters, Natural Hazards and Earth System Sciences, 17, 1159–1175, https://doi.org/10.5194/nhess-17-1159-2017, https://www.nat-hazards-earth-syst-sci.net/17/1159/2017/, 2017.

Marc, O., Behling, R., Andermann, C., Turowski, J. M., Illien, L., Roessner, S., and Hovius, N.: Long-term erosion of the Nepal Himalayas by bedrock landsliding: the role of monsoons, earthquakes and giant landslides, Earth Surface Dynamics, 7, 107–128, https://doi.org/10.5194/esurf-7-107-2019, https://www.earth-surf-dynam.net/7/107/2019/, 2019.

Martel, S.: Mechanics of landslide initiation as a shear fracture phenomenon, Marine Geology, 203, 319–339, https://doi.org/10.1016/S0025-3227(03)00313-X, http://linkinghub.elsevier.com/retrieve/pii/S002532270300313X, 2004.

Massa, M., Barani, S., and Lovati, S.: Overview of topographic effects based on experimental observations: meaning, causes and possible interpretations, Geophysical Journal International, 197, 1537–1550, https://doi.org/10.1093/gji/ggt341, https://academic.oup.com/gji/article-lookup/doi/10.1093/gji/ggt341, 2014.

Massey, C., Townsend, D., Rathje, E., Allstadt, K. E., Lukovic, B., Kaneko, Y., Bradley, B., Wartman, J., Jibson, R. W., Petley, D. N., Horspool, N., Hamling, I., Carey, J., Cox, S., Davidson, J., Dellow, S., Godt, J. W., Holden, C., Jones, K., Kaiser, A., Little, M., Lyndsell, B., McColl, S., Morgenstern, R., Rengers, F. K., Rhoades, D., Rosser, B., Strong, D., Singeisen, C., and Villeneuve, M.: Landslides Triggered by the 14 November 2016 Mw 7.8 Kaikoura Earthquake, New Zealand, Bulletin of the Seismological Society of America, 108, 1630–1648, https://doi.org/10.1785/0120170305, https://pubs.geoscienceworld.org/ssa/bssa/article/529881/Landslides-Triggered-by-the-14-November-2016-Mw78https://pubs.geoscienceworld.org/ssa/bssa/article/108/3B/1630/529881/Landslides-Triggered-by-the-14-November-2016-Mw78, 2018.

Matsumoto, J.: Heavy rainfalls over East Asia, International Journal of Climatology, 9, 407–423, https://doi.org/10.1002/joc.3370090407, http://doi.wiley.com/10.1002/joc.3370090407, 1989.

Maufroy, E., Cruz-Atienza, V. M., and Gaffet, S.: A Robust Method for Assessing 3-D Topographic Site Effects: A Case Study at the LSBB Underground Laboratory, France, Earthquake Spectra, 28, 1097–1115, https://doi.org/10.1193/1.4000050, http://earthquakespectra.org/doi/10.1193/1.4000050, 2012.

Maufroy, E., Cruz-Atienza, V. M., Cotton, F., and Gaffet, S.: Frequency-scaled curvature as a proxy for topographic site-effect amplification and ground-motion variability, Bulletin of the Seismological Society of America, 105, 354–367, https://doi.org/10.1785/0120140089, 2015.

McClung, D. M.: Fracture mechanical models of dry slab avalanche release, Journal of Geophysical Research: Solid Earth, 86, 10 783–10 790, https://doi.org/10.1029/JB086iB11p10783, http://doi.wiley.com/10.1029/JB086iB11p10783, 1981.

Meunier, P., Hovius, N., and Haines, A. J.: Regional patterns of earthquake-triggered landslides and their relation to ground motion, Geophysical Research Letters, 34, 1–5, https://doi.org/10.1029/2007GL031337, 2007.

Meunier, P., Hovius, N., and Haines, J. A.: Topographic site effects and the location of earthquake induced landslides, Earth and Planetary Science Letters, 275, 221–232, https://doi.org/10.1016/j.epsl.2008.07.020, http://dx.doi.org/10.1016/j.epsl.2008.07.020, 2008.

Meunier, P., Uchida, T., and Hovius, N.: Landslide patterns reveal the sources of large earthquakes, Earth and Planetary Science Letters, 363, 27–33, https://doi.org/10.1016/j.epsl.2012.12.018, http://dx.doi.org/10.1016/j.epsl.2012.12.018https://linkinghub.elsevier.com/retrieve/pii/S0012821X12007042, 2013.

Miles, S. B. and Keefer, D. K.: Evaluation of CAMEL - comprehensive areal model of earthquake-induced landslides, Engineering Geology, 104, 1–15, https://doi.org/10.1016/j.enggeo.2008.08.004, http://dx.doi.org/10.1016/j.enggeo.2008.08.004, 2009.

Moore, J. D. P., Yu, H., Tang, C.-H., Wang, T., Barbot, S., Peng, D., Masuti, S., Dauwels, J., Hsu, Y.-J., Lambert, V., Nanjundiah, P., Wei, S., Lindsey, E., Feng, L., and Shibazaki, B.: Imaging the distribution of transient viscosity after the 2016 M w 7.1 Kumamoto earthquake, Science, 356, 163–167, https://doi.org/10.1126/science.aal3422, http://www.sciencemag.org/lookup/doi/10.1126/science.aal3422, 2017.

National Research Institute for Earth Science and Disaster Prevention: Disaster Research Institute for Science and Technology Research Materials "1: 50,000 landslide topography map", http://dil-opac.bosai.go.jp/publication/nied{_}tech{_}note/landslidemap/index.html, 2014.

National Research Institute for Earth Science and Disaster Prevention: Sediment movement distribution map by the Kumamoto earthquake (updated in 2016.6.27), http://www.bosai.go.jp/mizu/dosha.html, 2016.

Newman, A. V. and Okal, E. A.: Teleseismic estimates of radiated seismic energy: The E/M 0 discriminant for tsunami earthquakes, Journal of Geophysical Research: Solid Earth, 103, 26 885–26 898, https://doi.org/10.1029/98JB02236, http://doi.wiley.com/10.1029/98JB02236, 1998.

Newmark, N. M.: Effects of Earthquakes on Dams and Embankments, Géotechnique, 15, 139–160, https://doi.org/10.1680/geot.1965.15.2.139, http://www.icevirtuallibrary.com/doi/10.1680/geot.1965.15.2.139, 1965.

Paudel, P. P., Omura, H., Kubota, T., and Devkota, B.: Characterization of terrain surface and mechanisms of shallow landsliding in upper Kurokawa watershed, Mt Aso, western Japan, Bulletin of Engineering Geology and the Environment, 67, 87–95, https://doi.org/10.1007/s10064-007-0108-z, http://link.springer.com/10.1007/s10064-007-0108-z, 2008.

Pawluszek, K. and Borkowski, A.: Impact of DEM-derived factors and analytical hierarchy process on landslide susceptibility mapping in the region of Rożnów Lake, Poland, Natural Hazards, 86, 919–952, https://doi.org/10.1007/s11069-016-2725-y, 2017.

Planchon, O. and Darboux, F.: A fast, simple and versatile algorithm to fill the depressions of digital elevation models, CATENA, 46, 159–176, https://doi.org/10.1016/S0341-8162(01)00164-3, http://linkinghub.elsevier.com/retrieve/pii/S0341816201001643, 2001.

Roback, K., Clark, M. K., West, A. J., Zekkos, D., Li, G., Gallen, S. F., Chamlagain, D., and Godt, J. W.: The size, distribution, and mobility of landslides caused by the 2015 M w 7.8 Gorkha earthquake, Nepal, Geomorphology, 301, 121–138, https://doi.org/10.1016/j.geomorph.2017.01.030, https://doi.org/10.1016/j.geomorph.2017.01.030http://linkinghub.elsevier.com/retrieve/pii/S0169555X1630719X, 2018.

Romeo, R.: Seismically induced landslide displacements: A predictive model, Engineering Geology, 58, 337–351, https://doi.org/10.1016/S0013-7952(00)00042-9, 2000.

Rudnicki, J. W. and Freund, L. B.: On energy radiation from seismic sources, Bulletin of the Seismological Society of America, 71, 583–595, http://dx.doi.org/, 1981.

Sato, T., Chigira, M., and Matsushi, Y.: Topographic and Geological Features of Landslides Induced by the 2016 Kumamoto Earthquake in the Western Part of the Aso Caldera, DPRI Annuals, 60B, 431–452, http://hdl.handle.net/2433/229383, 2017.

Savage, J. C.: Radiation from a realistic model of faulting, Bulletin of the Seismological Society of America, 56, 577–592, http://www.bssaonline.org/content/56/2/577.short, 1966.

Schnabel, P. B. and Bolton Seed, H.: Accelerations in rock for earthquakes in the western United States, Bulletin of the Seismological Society of America, 63, 501–516, 1973.

Schwarz, G.: Estimating the Dimension of a Model, The Annals of Statistics, 6, 461–464, https://doi.org/10.1214/aos/1176344136, http://projecteuclid.org/euclid.aos/1176344136, 1978.

Shoja-taheri, B. Y. J. and Anderson, J. G.: THE 1978 TABAS, IRAN, EARTHQUAKE: AN INTERPRETATION OF THE STRONG MOTION RECORDS, Bulletin of the Seismological Society of America, 78, 142–171, 1988.

Sidle, R. C. and Chigira, M.: Landslides and debris flows strike kyushu, japan, Eos, 85, https://doi.org/10.1029/2004EO150001, 2004.

Somerville, P., Irikura, K., Graves, R., Sawada, S., Wald, D., Abrahamson, N., Iwasaki, Y., Kagawa, T., Smith, N., and Kowada, A.: Characterizing Crustal Earthquake Slip Models for the Prediction of Strong Ground Motion, Seismological Research Letters, 70, 59–80, https://doi.org/10.1785/gssrl.70.1.59, http://srl.geoscienceworld.org/cgi/doi/10.1785/gssrl.70.1.59, 1999.

Somerville, P. G., Smith, N. F., Graves, R. W., and Abrahamson, N. a.: Modification of Empirical Strong Ground Motion Attenuation Relations to Include the Amplitude and Duration Effects of Rupture Directivity, Seismological Research Letters, 68, 199–222, https://doi.org/10.1785/gssrl.68.1.199, 1997.

Song, K., Wang, F., Dai, Z., Iio, A., Osaka, O., and Sakata, S.: Geological characteristics of landslides triggered by the 2016 Kumamoto earthquake in Mt. Aso volcano, Japan, Bulletin of Engineering Geology and the Environment, pp. 1–10, https://doi.org/10.1007/s10064-017-1097-1, http://link.springer.com/10.1007/s10064-017-1097-1, 2017.

Spudich, B. P., Chiou, B. S. J., Graves, R., Collins, N., and Somerville, P.: A Formulation of Directivity for Earthquake Sources Using Isochrone Theory, U.S. Geol. Surv. Open-File Rept. 2004-1268, p. 54, 2004.

Spudich, P. and Chiou, B. S. J.: Directivity in NGA earthquake ground motions: Analysis using isochrone theory, Earthquake Spectra, 24, 279–298, https://doi.org/10.1193/1.2928225, 2008.

Spudich, P., Bayless, J., Baker, J., Chiou, B. S. J., Rowshandel, B., Shahi, S., and Somerville, P.: Final Report of the NGA-West2 Directivity Working Group, Tech. Rep. Final, Pacific Earthquake Engineering Research Center, 2013.

Strasser, F. O., Arango, M. C., and Bommer, J. J.: Scaling of the Source Dimensions of Interface and Intraslab Subduction-zone Earthquakes with Moment Magnitude, Seismological Research Letters, 81, 941–950, https://doi.org/10.1785/gssrl.81.6.941, http://srl.geoscienceworld.org/cgi/doi/10.1785/gssrl.81.6.941, 2010.

Tang, R., Fan, X., Scaringi, G., Xu, Q., van Westen, C. J., Ren, J., and Havenith, H.-B.: Distinctive controls on the distribution of river-damming and non-damming landslides induced by the 2008 Wenchuan earthquake, Bulletin of Engineering Geology and the Environment, https://doi.org/10.1007/s10064-018-1381-8, http://link.springer.com/10.1007/s10064-018-1381-8, 2018.

Tarantola, A.: Inverse problem theory and methods for model parameter estimation, SIAM, 2005.

Taylor, S. R., Bonner, B. P., and Zandt, G.: Attenuation and scattering of broadband P and S waves across North America, Journal of Geophysical Research: Solid Earth, 91, 7309–7325, https://doi.org/10.1029/JB091iB07p07309, http://doi.wiley.com/10.1029/JB091iB07p07309, 1986.

Tinti, E., Fukuyama, E., Piatanesi, A., and Cocco, M.: A Kinematic Source-Time Function Compatible with Earthquake Dynamics, Bulletin of the Seismological Society of America, 95, 1211–1223, https://doi.org/10.1785/0120040177, https://pubs.geoscienceworld.org/bssa/article/95/4/1211-1223/121062, 2005.

Torgoev, A. and Havenith, H. B.: 2D dynamic studies combined with the surface curvature analysis to predict Arias Intensity amplification, Journal of Seismology, 20, 711–731, https://doi.org/10.1007/s10950-016-9553-0, http://dx.doi.org/10.1007/s10950-016-9553-0, 2016.

Travasarou, T., Bray, J. D., and Abrahamson, N. A.: Empirical attenuation relationship for Arias Intensity, Earthquake Engineering & Structural Dynamics, 32, 1133–1155, https://doi.org/10.1002/eqe.270, http://doi.wiley.com/10.1002/eqe.270, 2003.

Uchide, T., Horikawa, H., Nakai, M., Matsushita, R., Shigematsu, N., Ando, R., and Imanishi, K.: The 2016 Kumamoto–Oita earthquake sequence: aftershock seismicity gap and dynamic triggering in volcanic areas, Earth, Planets and Space, 68, 180, https://doi.org/10.1186/s40623-016-0556-4, http://earth-planets-space.springeropen.com/articles/10.1186/s40623-016-0556-4, 2016.

Wang, R., Schurr, B., Milkereit, C., Shao, Z., and Jin, M.: An Improved Automatic Scheme for Empirical Baseline Correction of Digital Strong-Motion Records, Bulletin of the Seismological Society of America, 101, 2029–2044, https://doi.org/10.1785/0120110039, http://www.bssaonline.org/cgi/doi/10.1785/0120110039, 2011.

Weber, B.: Tragwerksdynamik: Vorlesung, Sommersemester 2002, 2002.

Yagi, Y., Okuwaki, R., Enescu, B., Kasahara, A., Miyakawa, A., and Otsubo, M.: Rupture process of the 2016 Kumamoto earthquake in relation to the thermal structure around Aso volcano, Earth, Planets and Space, 68, 118, https://doi.org/10.1186/s40623-016-0492-3, http://earth-planets-space.springeropen.com/articles/10.1186/s40623-016-0492-3, 2016.

Yamada, M., Heaton, T., and Beck, J.: Real-Time Estimation of Fault Rupture Extent Using Near-Source versus Far-Source Classification, Bulletin of the Seismological Society of America, 97, 1890–1910, https://doi.org/10.1785/0120060243, https://pubs.geoscienceworld.org/bssa/article/97/6/1890-1910/341844, 2007.

Yamada, M., Kumagai, H., Matsushi, Y., and Matsuzawa, T.: Dynamic landslide processes revealed by broadband seismic records, Geophysical Research Letters, 40, 2998–3002, https://doi.org/10.1002/grl.50437, http://doi.wiley.com/10.1002/grl.50437, 2013.

Yamada, M., Mangeney, A., Matsushi, Y., and Matsuzawa, T.: Estimation of dynamic friction and movement history of large landslides, Landslides, d, 1–12, https://doi.org/10.1007/s10346-018-1002-4, http://link.springer.com/10.1007/s10346-018-1002-4, 2018.

Yoffe, E. H.: LXXV. The moving griffith crack, The London, Edinburgh, and Dublin Philosophical Magazine and Journal of Science, 42, 739–750, https://doi.org/10.1080/14786445108561302, http://www.tandfonline.com/doi/abs/10.1080/14786445108561302, 1951.

Yoshida, K., Miyakoshi, K., Somei, K., and Irikura, K.: Source process of the 2016 Kumamoto earthquake (Mj7.3) inferred from kinematic inversion of strong-motion records, Earth, Planets and Space, 69, 64, https://doi.org/10.1186/s40623-017-0649-8, http://earth-planets-space.springeropen.com/articles/10.1186/s40623-017-0649-8, 2017.

Yuan, R.-M., Deng, Q.-H., Cunningham, D., Xu, C., Xu, X.-W., and Chang, C.-P.: Density Distribution of Landslides Triggered by the 2008 Wenchuan Earthquake and their Relationships to Peak Ground Acceleration, Bulletin of the Seismological Society of America, 103, 2344–2355, https://doi.org/10.1785/0120110233, https://pubs.geoscienceworld.org/bssa/article/103/4/2344-2355/331645, 2013.

Zevenbergen, L. W. and Thorne, C. R.: Quantitative analysis of land surface topography, Earth Surface Processes and Landforms, 12, 47–56, https://doi.org/10.1002/esp.3290120107, http://doi.wiley.com/10.1002/esp.3290120107, 1987.